Using misorientation and weighted Burgers vector statistics to understand the intragranular boundary development and grain boundary formation at high temperatures

Sheng Fan[1*], John Wheeler[2], David J. Prior[1], Marianne Negrini[1], Andrew J. Cross[3], Travis F. Hager[4], David L. Goldsby[4]

[1] Department of Geology, University of Otago, Dunedin, New Zealand

[*] Present address: Department of Earth Sciences, University of Cambridge, Cambridge, UK.

[2] Department of Earth and Ocean Sciences, University of Liverpool, Liverpool, UK

[3] Department of Geology and Geophysics, Woods Hole Oceanographic Institution, Woods Hole, MA, USA

[4] Department of Earth and Environmental Science, University of Pennsylvania, Philadelphia, PA, USA

Corresponding author: Sheng Fan (`sheng.fan@otago.ac.nz`)

Key Points:

- Crystallographic geometry of intragranular boundaries quantified using misorientation and weighted Burgers vector statistics
- Intragranular boundaries can form via intersection of segments produced by recovery of dislocations with distinct slip systems
- Subgrain rotation alone cannot change the crystallographic geometry of boundaries; extra processes contribute upon grain boundary formation

Abstract

Strain weakening during plastic deformation can be achieved via strain energy reduction due to intragranular boundary development and grain boundary formation. To examine intragranular boundary formation at high temperatures ($T_h \approx 0.9$), we analysed electron backscatter diffraction (EBSD) data of coarse-grained ice deformed at -30°C. Misorientation and weighted Burgers vector (WBV) statistics were calculated along planar intragranular boundaries. Neighbour-pair and random-pair misorientation distributions intersect at misorientation angles of 10–30°, indicating an upper limit to the misorientation threshold angle at which neighbouring grains begin to interact, e.g., rotate relative to each other. Misorientation angles change markedly along each analysed intragranular boundary, linking low- (<10°) and high-angle (10–38°) segments, with each segment exhibiting distinct misorientation axes and WBV directions.

We suggest that these boundaries might be produced by the growth and intersection of individual boundary segments comprised of dislocations with distinct slip systems. This new kinematic model does not require a change in the boundary geometry after its formation, as required by the other models, to modify the crystallographic geometry of a planar boundary. Misorientation axis distributions are fundamentally different between intragranular boundaries (mostly confined to the ice basal plane) and grain boundaries (largely dispersed). This observation suggests a strong crystallographic control of intragranular boundary development via subgrain rotation. The apparent lack of crystallographic control for grain boundaries, on the other hand, suggests that misorientation axes become randomized upon grain boundary formation, likely due to the operation of other mechanisms/processes that can modify misorientation axes.

Plain Language Summary

Ice and other minerals usually develop widespread boundaries within grains. Laboratory experiments show these intragranular boundaries are the manifestation of crystalline defects ("dislocations"). During deformation, intragranular boundaries will develop from low-angle to high-angle via a continuous input of dislocations, and they might enclose and transform into grain boundaries. These processes cause minerals to weaken, affecting their large-scale flow. To understand intragranular boundary development and grain boundary formation at temperatures close to minerals' melting points, we deformed ice samples at -30°C. The microscopic structure of the deformed ice samples was examined using an electron microscope. We found a widespread variation of crystallographic geometry along individual intragranular boundaries; such observation cannot be explained by previous models. The formation of these boundaries can be better explained by an intersection of segments with distinct crystallographic geometry; this model does not require a change of spatial boundary geometry. The rotation axes of intragranular boundaries are within crystallographic basal plane, whilst grain boundaries have a random rotation axes distribution. This observation suggests that grain boundaries are subject to other mechanisms/processes that can modify a boundary's crystallographic geometry—such modifications cannot be achieved by intracrystalline rotation alone.

1 Introduction

We must understand the microstructural evolution of crystalline materials to explain their strength evolution and its large-scale consequences. Deformed rock and ice samples commonly exhibit networks of intragranular boundaries—planar defects defined by a sharp change in crystal lattice orientation—that begin developing at very low strains (usually beyond ~2%) and become increasingly widespread as deformation progresses (Fan et al., 2020; Trimby et al., 1998; Valcke et al., 2006; White, 1976). Intragranular boundaries are composed of ar-

rays of dislocations—a type of crystalline line defect that accommodates plastic strain through glide and climb (Orowan, 1934; Polanyi, 1934; Taylor, 1934)—and can be described by misorientation angle, misorientation axis, slip plane, and slip direction. During high-temperature creep, the misorientation angle of a given intragranular boundary increases as dislocations of the same polarity are continuously added, a process termed subgrain rotation (Halfpenny et al., 2006). Subgrain rotation is often used to explain the formation of subgrain boundaries and kink bands, which are two sub-types of intragranular boundary (Bell et al., 1986; Poirier & Nicolas, 1975; Urai et al., 1986). When the misorientation angle across an intragranular boundary becomes large enough (generally considered as 10°), the crystalline structure of the boundary becomes sufficiently disordered that it can no longer be described as a simple array of dislocations. Consequently, the (low-angle) intragranular boundary becomes a (high-angle) grain boundary. This process, known as subgrain rotation recrystallization, results in the formation (nucleation) of new "recrystallized" grains at the expense of old, highly strain relict grains. Through subgrain rotation recrystallization, the internal stress state of a material is lowered, thereby counteracting work hardening due to dislocation multiplication and entanglement. Consequently, strain weakening can be achieved, which is necessary for the formation of narrow localised shear zones (Rutter, 1999; Skemer et al., 2009; Tullis & Yund, 1985).

The transformation from an intragranular boundary to a grain boundary requires an increasing intragranular boundary misorientation angle up to a threshold, above which organised dislocation arrays do not exist (Read & Shockley, 1950). Quantifying the grain boundary threshold angle is essential for an accurate grain size measurement. A lower grain boundary threshold angle will probably increase the apparent density of grain boundaries (length per unit area), leading to an underestimation of average grain size (Trimby et al., 1998; Wheeler et al., 2003). For minerals such as olivine and quartz, the grain boundary threshold angle has been constrained by transmission electron microscopy (TEM) (Heinemann et al., 2005; McLaren, 1991; Shigematsu et al., 2006). However, the grain boundary threshold angle in ice remains unclear—previous studies use various grain boundary thresholds from 5° (Weikusat et al., 2017), to 7° (Chauve et al., 2017), to 10° (Fan et al., 2020) for ice microstructure analyses. Even though grain size statistics are generally very similar for imposed grain boundary threshold angles of 5–30° (details provided in Appendix A), it is still important to constrain the ice grain boundary threshold angle for a more accurate calculation of average grain size—a crucial parameter when calculating the strength of glacial and polar ices deforming via grain size sensitive creep (Goldsby & Kohlstedt, 2001; Goldsby, 2006).

Intragranular boundaries also preserve key information about the dislocations that comprise them (Lloyd et al., 1997; Poirier, 1976; Prior et al., 2002; Trimby et al., 1998). The direction and minimum amount of lattice displacement caused by dislocation movement can be quantified by the Burgers vector (Burgers, 1940). Based on the relation between directions of the dislocation line and

the Burgers vector, an intragranular boundary composed of dislocations can be split into two end-member types (Burgers, 1940; Nabarro, 1967). Tilt boundaries are composed predominantly of edge dislocations, and have rotation (i.e., misorientation) axes lying within the boundary plane (Figs. 1(a), 1(b)). Twist boundaries, on the other hand, are composed predominantly of screw dislocations, and have misorientation axes perpendicular to the boundary plane (Figs. 1(c), 1(d)). Pure twist boundaries need to contain dislocations with at least two distinct Burgers vector directions (Fig. 1(d)).

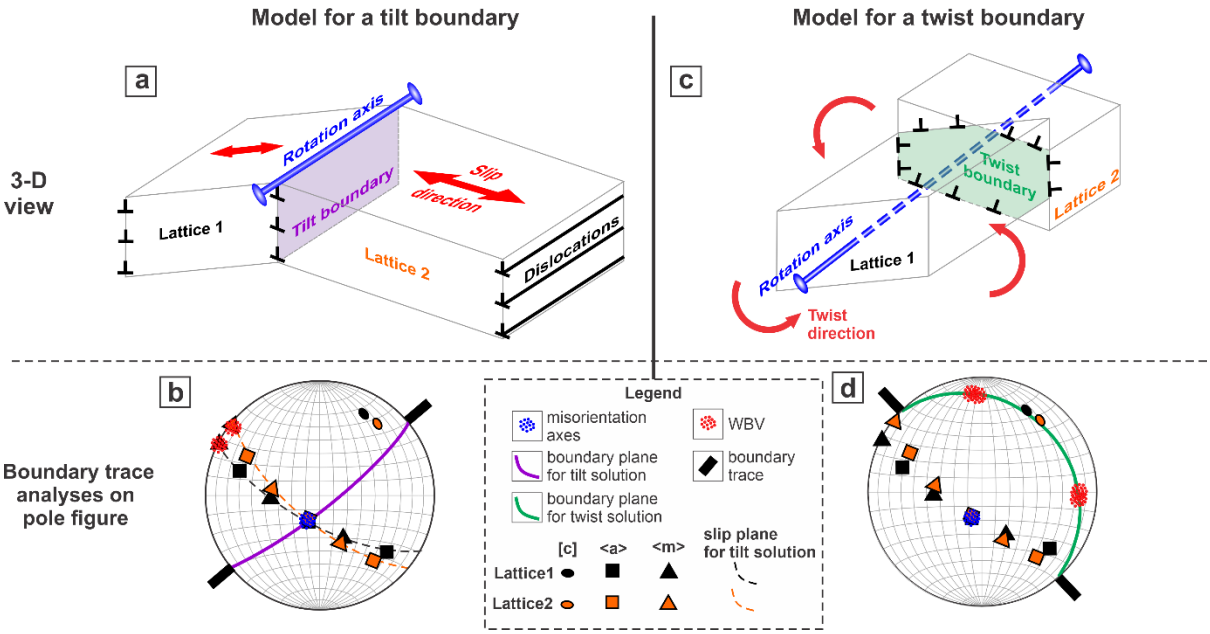

Figure 1. Illustration of principles of the two end-member boundary type models of pure tilt boundary (left column), and pure twist boundary (right column). (a), (b) Tilt boundary has misorientation axes (blue dots) lying within the boundary plane (purple great circle). (c), (d) Twist boundary has misorientation axes perpendicular to the boundary plane (green great circle), and it needs to contain dislocations with at least two distinct Burgers vector (red dots) directions.

In this study, we aim at:

(1) Understand the processes that lead to intragranular boundary development during high temperature creep. Here we examine deformed ice, which we treat as an analogue for major rock-forming minerals, namely quartz and olivine. Ice has crystal symmetry very similar to that of quartz (Wilson et al., 2014) and also exhibits strong viscous anisotropy, like olivine (Hansen et al., 2012). Moreover, many rock-forming minerals have melting temperatures that are difficult to reach in the laboratory (e.g., quartz: 1950 K; olivine: 2200 K). In contrast, high-temperature (T_h 0.9) ice deformation can be easily achieved. Studying ice deformation is also important in itself for understanding glacial ice dynamics.

(2) Investigate the crystallographic geometry (i.e., misorientation axes and slip directions) of intragranular boundaries through their formation, growth, and ultimate transformation into grain boundaries. The stereological bias of boundary misorientation axes and slip directions measured from a 2-D sample surface has been tested before they were used for constraining boundary crystallographic geometry. Previous studies have suggested that at relatively low temperatures ($T_h < 0.7$), subgrain rotation may produce CPO weakening (Lopez-Sanchez et al., 2021). However, the role of subgrain rotation on modifying boundary structure at high temperatures remains unclear.

(3) Quantify the threshold misorientation angle that defines the transition from intragranular (subgrain) boundaries to intergranular (grain) boundaries in ice. This is essential for a more accurate measurement of ice grain size, which is the key input for a grain size sensitive flow law (Goldsby & Kohlstedt, 2001) that can be used to predict the mechanical behaviour (e.g., strain rate and/or stress) of ice flow.

We used statistics of misorientation axes and sampled Burgers vectors calculated from EBSD data, which were collected from a 2-D surface, to understand intragranular boundary geometry in 3-D. We present detailed intragranular boundary analyses across intragranular boundaries observed within deformed coarse-grained (~1300 µm) ice samples. These samples, which were previously described by Fan, Prior, Hager, et al. (2021), show a widespread development of recrystallized grains, and intragranular boundaries comprised of both high-angle ($> 10°$) and low-angle (4–10°) components (Figs 2(a)–2(b)). Moreover, the samples are much coarser grained (average starting grain size of ~1300 µm) than our measuring resolution (5 µm). As such, we are able to resolve intragranular features in fine detail and achieve our three aims.

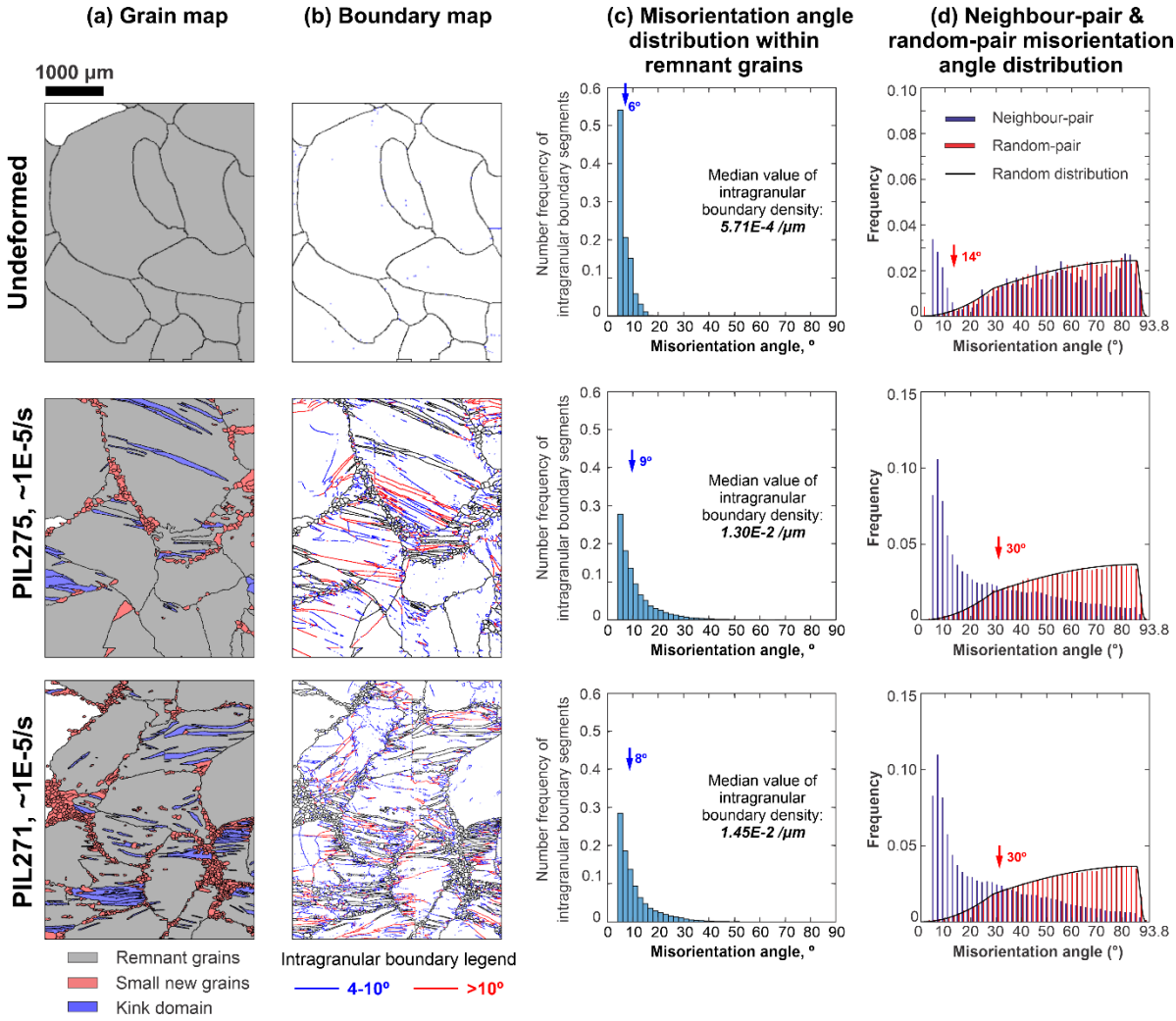

Figure 2. Summary of microstructural statistics for ice samples used in this study. The original data are provided in Fan, Prior, Hager, et al. (2021). (a) Grain map for grain populations. (b) Boundary map. The grain boundary is black. (c) Misorientation angle distribution for intragranular boundaries within remnant grains. The vertical blue arrow represents the median misorientation angle for intragranular boundaries with misorientation angles larger than 4°. (d) Neighbour-pair (blue bars) and random-pair (red bars) misorientation angle distributions. Misorientation angle distribution calculated for randomly distributed ice 1 h crystals are shown with a black line. Red arrow indicates the misorientation angle, at which neighbor-pair and random-pair misorientation distributions intersect with each other.

2 Method

2.1 Ice deformation experiments and EBSD data acquisition

Coarse-grained ice samples—which exhibit a homogeneous microstructure, with few intragranular boundaries and a starting average grain size of ~1300 µm—were fabricated using a "flood-freeze" method (Cole, 1979) These ice samples were deformed within confined (~40 MPa) nitrogen gas medium at -30 °C under constant displacement rates, yielding true axial strain rates of $\sim 1 \times 10^{-5}$ (sample no. PIL275) and $6 \times 10^{-5} s^{-1}$ (sample no. PIL271), to ~10% true axial strain. Full details of the sample fabrication and deformation experiments are provided in (Fan, Prior, Hager, et al., 2021) (see also Appendix B).

We prepared the ice samples, and acquired cryo-EBSD data, following the procedures described by Prior and others (2015). EBSD maps were indexed (as ice-1h) at a typical rate of 90% under the "speed 2" mode (8x8 detector binning), with a maximum frame rate (acquired pixels per second) of ~1500 Hz. Full details of the EBSD data acquisition are provided in (Fan, Prior, Hager, et al., 2021), and are summarized in Appendix C.

During sample extraction, transportation, and preparation for cryo-EBSD, post-deformation microstructural modifications may occur. Possible changes include normal grain growth, crystallographic preferred orientation (CPO) evolution, and changes in the geometry—both in sample and crystallographic reference frames—of intragranular boundaries. However, as discussed elsewhere, such changes are likely negligible over the short timescales (within 30 minutes at $T <$ -20°C) involved here (Fan, Prior, Cross, et al., 2021; Fan, Prior, Hager, et al., 2021; Hidas et al., 2017; Wilson et al., 2014).

2.2 EBSD data denoising and grain construction

Grain construction and denoising were performed using the MTEX toolbox within MATLAB. First, we constructed ice grains from raw EBSD pixel maps using a Voronoi decomposition algorithm (Bachmann et al., 2011). Duplicated data points—a common montage-related artefact—usually limited to a strip of 1-2 pixels in width, are observed along the stitches of adjacent tiles in montaged maps (Fan, Prior, Hager, et al., 2021). We eliminated duplicated data points at stitches by simply removing these repeated pixels. Grain boundaries were initially defined using a 10° misorientation threshold angle. Grains that are likely to result from mis-indexing (with less than 4 pixels indexed as ice-1h) or poorly constrained (with <50% indexed pixel coverage) were removed. After that, we applied the MTEX *fill* function on the denoised EBSD data to replace each non-indexed pixel with the nearest pixel indexed as ice-1h. During this step, the interpolated pixels populates 5–8% of the map area (Fan, Prior, Hager, et al., 2021). Finally, we reconstructed grains using the denoised, interpolated EBSD data with the boundary misorientation angle threshold of 10°. We note that,

pixels along some of the intragranular boundaries might not be indexed under the fast frame rate of EBSD data acquisition as used in this study (maximum ~1500 Hz, 8x8 camera binning). These pixels are likely to be indexed under slow frame rate (maximum ~100 Hz, no camera binning), which is much more time-consuming compared with fast frame rate. We chose the fast frame rate for our EBSD data collection due to a limited SEM time. However, the geometry of intragranular boundaries, including 2-D boundary trace, misorientation axes, and sampled Burgers vectors, are very similar between interpolated EBSD data collected under fast frame rate and real, non-interpolated EBSD data collected under slow frame rate (Appendix D). Therefore, we suggest the interpolation of EBSD pixel data is unlikely to introduce artefacts to the real geometry of intragranular boundaries.

2.3 Misorientation measurements and sampling of Burgers vectors

2.3.1 Misorientation angle and axes

Grain construction (Sect. 2.2) involves simple use of misorientation angles, but we are interested in details of how misorientations vary along particular boundaries because those variations carry information on boundary formation processes. However, boundaries calculated from EBSD pixel data comprise individual segments drawn between pixels with misorientation angles larger than a certain threshold (Figs. 3(a), 3(b)). Due to the square shape of each pixel collected in this study, boundary elements appear artificially pixelated (Figs. 3(a), 3(b)). To address this issue, for each boundary element we extracted the misorientation angle and x-y coordinates of its mid-point (illustrated as red triangle in Fig. 3(a)). The distance between the mid-points of adjacent boundary elements is then summed (Fig. 3(a)) so that we can plot the misorientation angle as a function of distance along the boundary from a reference starting point (e.g., black square mark in Fig. 3(b)) (Fig. 3(c)). Measurements across boundaries with lower misorientation angles usually contain higher angular errors on misorientation axes (Prior, 1999). Conventional EBSD measurements with low misorientation angles have large misorientation axis errors (Prior, 1999). Figure 3(d) illustrates maximum angular errors of representative misorientation axes with different misorientation angles (from Table 2 of Prior et al. (1999)). Therefore, intragranular boundaries with misorientation angles lower than 4° were not included in the analyses.

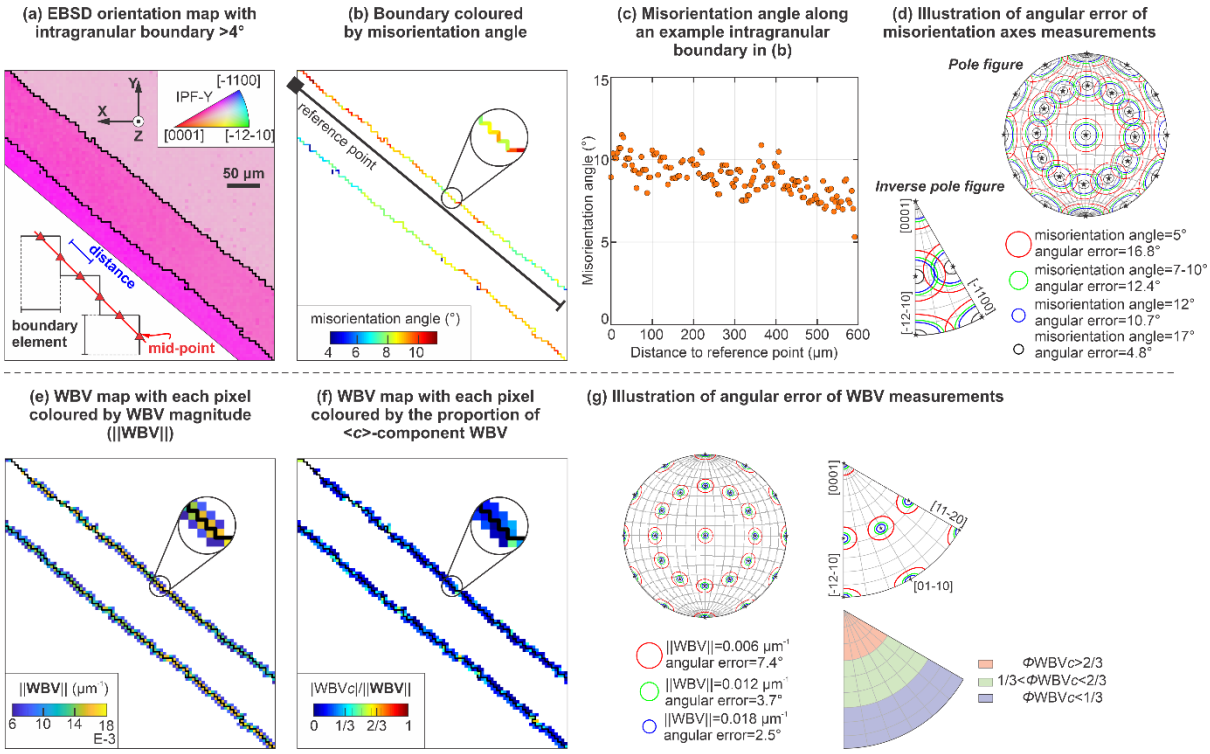

Figure 3. Illustration of principles of misorientation and WBV measurement methods applied in this study. (a) Orientation map of a sub-area chosen from the EBSD map of PIL275. Orientation map is coloured by IPF-Y, which uses the colour map to indicate the crystallographic axes that are parallel to the y-axis as shown by the black arrows. Boundaries with misorientation angles higher than 4° are shown black. Measurement of distances between adjacent boundary segments is illustrated in the bottom left corner. (b) Boundary map with each boundary segment coloured by the corresponding misorientation angle calculated from full crystallographic axes. (c) Misorientation angle as a function of distance between each boundary segment and boundary segment at the reference point shown in (b). (d) Illustration of maximum angular errors of representative misorientation axes (black dots) adapted from the Table 2 of Prior et al. (1999). (e) Weighted Burgers vector (WBV) map showing pixels with the magnitude of WBV (WBV) greater than 0.006 µm^{-1}. These pixels are coloured by their corresponding WBV. Boundaries are shown black. (f) Weighted Burgers vector (WBV) map showing pixels with WBV greater than 0.006 µm^{-1} coloured by the proportion of $<c>$-component WBV (ϕWBVc= WBVc/WBV). Boundaries are shown black. (g) Illustration of maximum angular errors of representative WBVs (black dots) with WBV of 0.006-0.018 µm^{-1} in PF and IPF, and areas in IPF corresponding to different ϕWBVc value ranges.

2.3.2 Sampling Burgers vectors

The geometries of smoothly curved lattices, or sharp changes in lattice orientation (intragranular boundaries) can be described in terms of geometrically necessary dislocations (GNDs) (Ashby, 1970). Hence, useful information on GNDs can in principle be obtained from EBSD data. The Weighted Burgers vector (WBV) method provides a mathematical, quantitative, and convenient tool to sample Burgers vectors from 2-D conventional EBSD maps (Wheeler et al., 2009).

WBV provides the sum of Burgers vectors over a given region of interest (Wheeler et al., 2009). Specifically, WBV measures the density of dislocation lines that intersect with the mapped 2-D section, where each dislocation line has its own Burgers vector. Dislocation lines lying within the plane of the section (or at low angles to it) have a much smaller apparent Burgers vector than dislocation lines perpendicular (or at a high angle) to the section. Thus, WBV is weighted towards dislocations that lie high angles to the section of interest.

For each pixel, we calculated the "differential" form of WBV from local crystal lattice orientation gradients; the "differential" form uses all indexed pixels within a selected region (Wheeler et al., 2009). We note that, WBV can also be calculated using an "integral" form, which calculates an averaged WBV within selected region using numerical integration (Wheeler et al., 2009). The "differential" form and "integral" form share the same mathematical foundation and are complementary to each other (Wheeler et al., 2009). Thus, in this study, we only present the WBV statistics calculated from the "differential" form.

Pixels on each side of boundaries usually show a relatively high magnitude of WBV (**WBV**) due to a high density of GNDs (Fig. 3(e)). It is worth noting that, pixels with high **WBV** are not equivalent to boundaries in this study. Boundaries are line elements that separate pixels, whereas WBV values are calculated for the pixels themselves. Figure 3(g) illustrates maximum angular errors of representative measurements with different **WBV**. Measurements with lower **WBV** generally correspond to a higher angular error (Wheeler et al., 2009). In this study, we choose pixels with **WBV** higher than 0.006 μm^{-1} for most analyses, as a compromise between having enough WBV measurement points with relatively low angular errors. However, for some of the intragranular structures, we chose pixels with **WBV** higher than 0.003 μm^{-1} if the number of pixels with **WBV** > 0.006 μm^{-1} is too small. The **WBV** thresholds of 0.003 and 0.006 μm^{-1} for defining low-error measurements is equivalent to a misorientation angle of ~1° and 2°, respectively, with a EBSD step size of 5 µm, and they are at least two times higher than the angular error of conventional EBSD orientation measurement (0.5–1°; Wallis et al., 2016). In fact, the patterns of WBV, i.e., WBV directions on inverse pole figure and pole figure, are very similar between measurements with **WBV** thresholds of 0.003, 0.006 µm and 0.012 μm^{-1} (equivalent to a misorientation angle of ~3.5°) (Sect. S1 of supplement).

The WBV analyses do not assume the activity of any particular Burgers vectors—WBV vectors can lie anywhere in crystal space (Wheeler et al., 2009). Thus, for each pixel, we can calculate the WBV over an imposed lattice component of the hexagonal ice-1h crystal, specifically—the [0001] (c-axis) in this study—to acquire a WBV component parallel to the c-axis—WBVc (Chauve et al., 2017; Piazolo et al., 2015; Wheeler et al., 2009). The ratio between magnitudes of WBVc (**WBV*c***) and WBV (**WBV**)—which we term ϕWBVc—enables us to quantify the relative contributions of Burgers vectors that are sub-parallel to the ice basal plane and Burgers vectors that are sub-parallel to non-basal directions to the total lattice displacements (e.g., Fig. 3(f)). The value of ϕWBVc ranges from 0 (when the directions of sampled Burgers vectors are parallel to the ice basal plane) to 1 (when the directions of sampled Burgers vectors are parallel to [0001] c-axis). Chauve et al. (2017) applied ϕWBVc value ranges of ϕWBVc <1/3, 1/3< ϕWBVc <2/3 and ϕWBVc >2/3 to separate WBVs that are dominated by <a>-component, <a+c>-component and <c>-component, respectively (Fig. 3(g)); these ϕWBVc value categories were adopted in this study.

2.3.3 Boundary trace analyses

Intragranular (low-angle) boundaries can be described by an array of dislocations, but (high-angle) grain boundaries are more disordered—in other words, (high-angle) grain boundaries are more difficult to describe in terms of individual dislocation types. In general, intragranular boundaries can be defined between two end-member cases: pure tilt boundaries and pure twist boundaries (Fig. 1; Sect. 1), depending on whether they are comprised predominately of edge or screw dislocations, respectively (Lloyd et al., 1997; Poirier, 1985). Constraining the crystallographic geometry of a crystalline boundary requires five macroscopic parameters (Goux, 1974; Saylor et al., 2003). Three of the parameters describe the rotation axis (plunge, azimuth) and angle required to rotate the crystal lattice on one side of the boundary to coincide with the crystal lattice on the other side of the boundary. The other two parameters describe the boundary plane orientation (plunge and azimuth of an axis normal to the boundary plane).

Boundary trace analysis (Lloyd et al., 1997) provides a means for constraining the geometry of individual boundary segments through knowledge of the boundary rotation (i.e., misorientation) axis, boundary trace (i.e., azimuth of the boundary on a 2-D section), and slip direction (i.e., Burgers vector). In many previous studies, Burgers vectors were not independently determined, so trace analyses rested on geometric assumptions about the orientations of the Burgers vector with respect to the boundary trace and misorientation axes (e.g., Seidemann et al., 2020). However, in this study, the Burgers vectors used for boundary trace analyses were independently sampled and determined using the WBV method (Sect. 2.3.2). Thus, our quantification of intragranular boundary geometry does not contain any assumption about the Burgers vector orienta-

tions.

Boundary trace analysis has proven particularly useful for studying intragranular boundaries, because it can determine whether a given pair of (misoriented) crystal lattice orientations are more likely separated by either a pure tilt or pure twist boundary (Chauve et al., 2017; Linckens et al., 2016; Piazolo et al., 2008; Prior et al., 2002; Seidemann et al., 2020). For the tilt boundary case, the sampled Burgers vector should lie outside the estimated tilt boundary plane range (transparent purple sphere), which is constrained by (1) measured boundary trace (heavy black bars stick out of primitive circle) and (2) misorientation axes (blue dots) on pole figure in the sample reference frame (Fig. 1(b)). For the twist boundary case, the sampled Burgers vector should lie within the estimated twist boundary plane range (green great circles), which are planes that are (1) normal to the misorientation axes (blue dots) and (2) constrained by measured boundary trace on pole figure in the sample reference frame (Fig. 1(d)).

The rotation axis is usually determined as the misorientation axis showing the least dispersion of orientations in previous studies (Boyle et al., 1998; Mainprice et al., 1993; Piazolo et al., 2008; Prior et al., 2002; Seidemann et al., 2020). EBSD data, which includes the information of full crystallographic axes, enables an easy access to the calculation of misorientation axes and angle (Sect. 2.3.1) (Fan et al., 2020; Prior, 1999; Wheeler et al., 2001). The determination of misorientation axes is more uncertain if the dispersion of crystallographic axes is very small or more than one crystallographic axis show similar degrees of dispersions (e.g., Fig. 3 in Piazolo et al., 2008). Thus, to highlighted the misorientation axes for low-angle intragranular boundaries, some studies directly plot point or contoured misorientation axes along intragranular boundaries on pole figures (Reddy & Buchan, 2005; Vaughan, 2017).

The 3-D boundary plane orientation can be hard to determine from 2-D EBSD data, because strongly curved and/or irregular non-planar boundaries in 2-D usually correspond to complex 3-D geometry so that the dip of boundary plane is hard to be constrained (Hammes & Peternell, 2018; Stechmann et al., 2016). Constraining a complex 3-D boundary geometry from 2-D data requires additional inputs, such as electron backscattered patterns (EBSPs) or electron channelling patterns (ECPs) (Lloyd et al., 1997, 2021). In this study, we selected intragranular boundaries that are mostly straight or only slightly curved for analyses, because straight boundaries on 2-D EBSD maps should correspond to approximately planar structures in 3-D. Thus, planar boundary planes can be simply constrained from 2-D boundary trace analyses without requiring more sophisticated 3-D data.

3 Testing the stereological impact on misorientation and WBV measurements

In this study, we use misorientation and WBV statistics calculated from EBSD data collected from a 2-D surface to understand intragranular boundary geometry in 3-D (Sects. 1, 2.2, 2.3). However, 2-D microstructural data might contain stereological biases—microstructural statistics captured from 2-D surfaces might not fully represent the real situation in 3-D (Underwood, 1973). Therefore, it is important to test the impact of stereological biases on intragranular distortion measurements (i.e., misorientation and WBV statistics) before these data were used to understand the 3-D geometry of intragranular boundaries.

For simplicity in the section, we make the following assertions:

(a) The misorientation axes (expressed in crystal coordinates) and angle should be the same regardless of the section plane.

(b) The WBV (expressed in crystal coordinates) may differ between section planes. Although the Burgers vectors of individual dislocation lines will be the same, the WBV is biased towards dislocation lines at high angles to the section plane. One can envisage a dislocation line at a low angle to one section plane (hence not contributing much) being at a high angle to another section plane (hence contributing a lot).

(c) Despite this, if we hypothesise that a boundary is made from a single type of dislocation, the WBV direction (expressed in crystal coordinates) will be the same regardless of the section plane. The WBV magnitude will be influenced by stereology.

To test the stereological impact on misorientation and WBV statistics, we extracted a cuboid ice slice from sample PIL271 (Fig. 4(a)) and collected EBSD data from two orthogonal surfaces of the cuboid ice slice following the procedures described in Sect. 2.2 (Fig. 4(b)). We firstly collect EBSD data from a polished surface parallel to the compression axis ("surface 1") (Figs. 4(b), 4(c)). After that, we carefully polished the orthogonal plane of "surface 1" for ~500 µm; EBSD data were then collected from this second polished surface ("surface 2"), which is normal to compression (Figs. 4(b), 4(c)). EBSD pixel maps of "surface 1" and "surface 2" were both coloured by crystal orientation with respect to the compression axis (i.e., IPF-σ_1) to aid in the identification of individual grains with clear intragranular boundaries captured on both orthogonal surfaces (Fig. 4(c)). From this procedure, we identified two sets of intragranular boundaries within the surfaces that are parallel and normal to compression using their positions along the intersection line: (1) B1(p) and B1(n); (2) B2(p), B2-1(n), and B2-2(n), where (p) indicates the surface is parallel to compression; (n) indicates the surface is normal to compression (Fig. 4(d)).

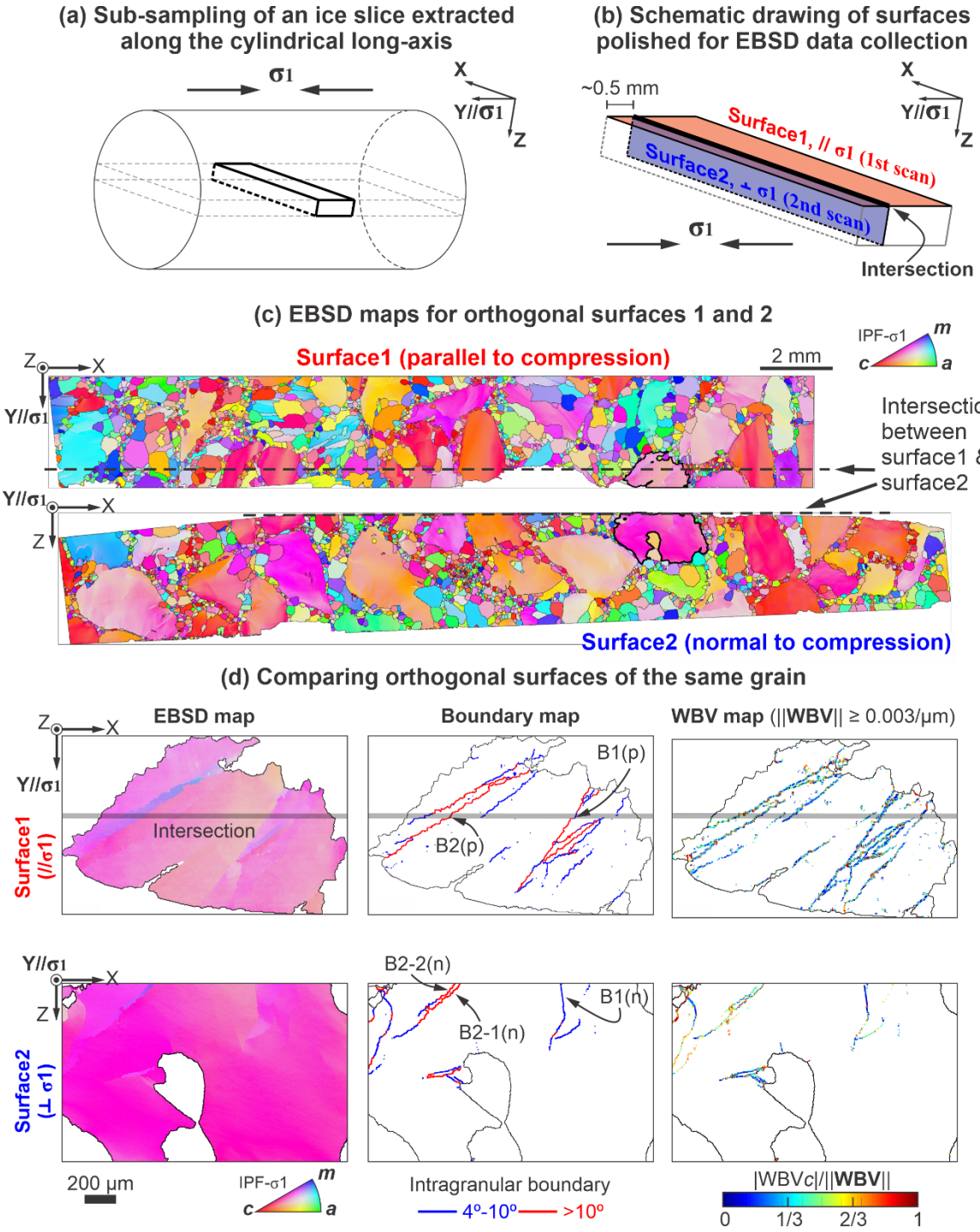
(a) Sub-sampling of an ice slice extracted along the cylindrical long-axis
σ1
X
Y//σ1
Z
(b) Schematic drawing of surfaces polished for EBSD data collection
~0.5 mm
Surface1, // σ1 (1st scan)
Surface2, ⊥ σ1 (2nd scan)
Intersection
(c) EBSD maps for orthogonal surfaces 1 and 2
Surface1 (parallel to compression)
2 mm
IPF-σ1
m
c
a
Intersection between surface1 & surface2
Surface2 (normal to compression)
(d) Comparing orthogonal surfaces of the same grain
EBSD map
Boundary map
WBV map (||WBV|| ≥ 0.003/μm)
Surface1 (//σ1)
Intersection
B1(p)
B2(p)
Surface2 (⊥ σ1)
B2-2(n)
B1(n)
B2-1(n)
200 μm
Intragranular boundary
4°-10°
>10°
|WBVc|/||WBV||
0
1/3
2/3
1

Figure 4. Testing the stereological impact on misorientation and WBV analyses. (a) Schematic drawing showing the geometry of subsampling a cuboid ice slice from sample PIL271. (b) Schematic drawing showing orthogonal surfaces polished for EBSD data collection. (c) EBSD pixel maps of orthogonal surfaces. The EBSD maps are coloured by IPF-Y, which uses the colour map to indicate the crystallographic axes that are parallel to the shortening axis (y-axis) as shown by the black arrows. (d) Microstructural maps of a grain with clear intragranular boundaries captured on both orthogonal surfaces.

Figure 5 demonstrates that intragranular boundaries exhibit similar misorientation axes and WBV, regardless of the section orientation:

For B1(p) and B1(n), the misorientation axes distributions on inverse pole figures (IPFs) generally lie very close to or possibly within the ice basal plane, with misorientation axes clustering near the *m*-axes (rows 1, 2; Figs. 5(a), 5(d)). The values of ϕWBVc (**WBV*c*/WBV**) on orthogonal surfaces are generally lower than 1/3 for pixels across B1 (rows 1, 2; Figs. 5(b), 5(f)). Many WBVs have directions close to the *a*-axes (rows 1, 2; Figs. 5(e)); however, WBV directions are slightly more scattered on the surface parallel to compression (B1(p)) than on the surface normal to compression (B1(n)) (compare row 1 and row 2; Fig. 5(e)).

For B2(p), B2-1(n), and B2-2(n), the misorientation axes distributions on IPFs generally lie very close to or possibly within the ice basal plane, with misorientation axes clustering near the *a*-axes (rows 3–5; Figs. 5(a), 5(d)). The values of ϕWBVc on orthogonal surfaces are generally higher than 1/3, with many of them between 1/3 and 2/3 for pixels across B2 (rows 3–5; Figs. 5(b), 5(f)). Many WBV across B2 have directions that are half-way between ice basal plane and *c*-axes on orthogonal surfaces (rows 3–5; Figs. 5(e)).

Observations in the last three paragraphs suggest:

(1) The misorientation axes distributions on the inverse pole figure (IPF) are very similar on orthogonal surfaces. This is in accord with Assertion (a) above.

(2) The values of ϕWBVc are very similar on orthogonal surfaces. This is a manifestation of Assertion (c) above.

(3) WBVs generally have directions that are close to rational crystallographic axes on orthogonal surfaces. In this study, we refer crystallographic axes with low Miller indices (e.g., *a*-axes [11-20], poles to the *m*-plane [10-10]) as rational crystallographic axes. This is a likely manifestation of Assertion (b) above.

In short, these analyses suggest that stereological impacts are negligible for misorientation and WBV statistics for individual boundaries. 2-D misorientation and WBV measurements are therefore reliable for understanding the 3-D geometry of individual boundaries.

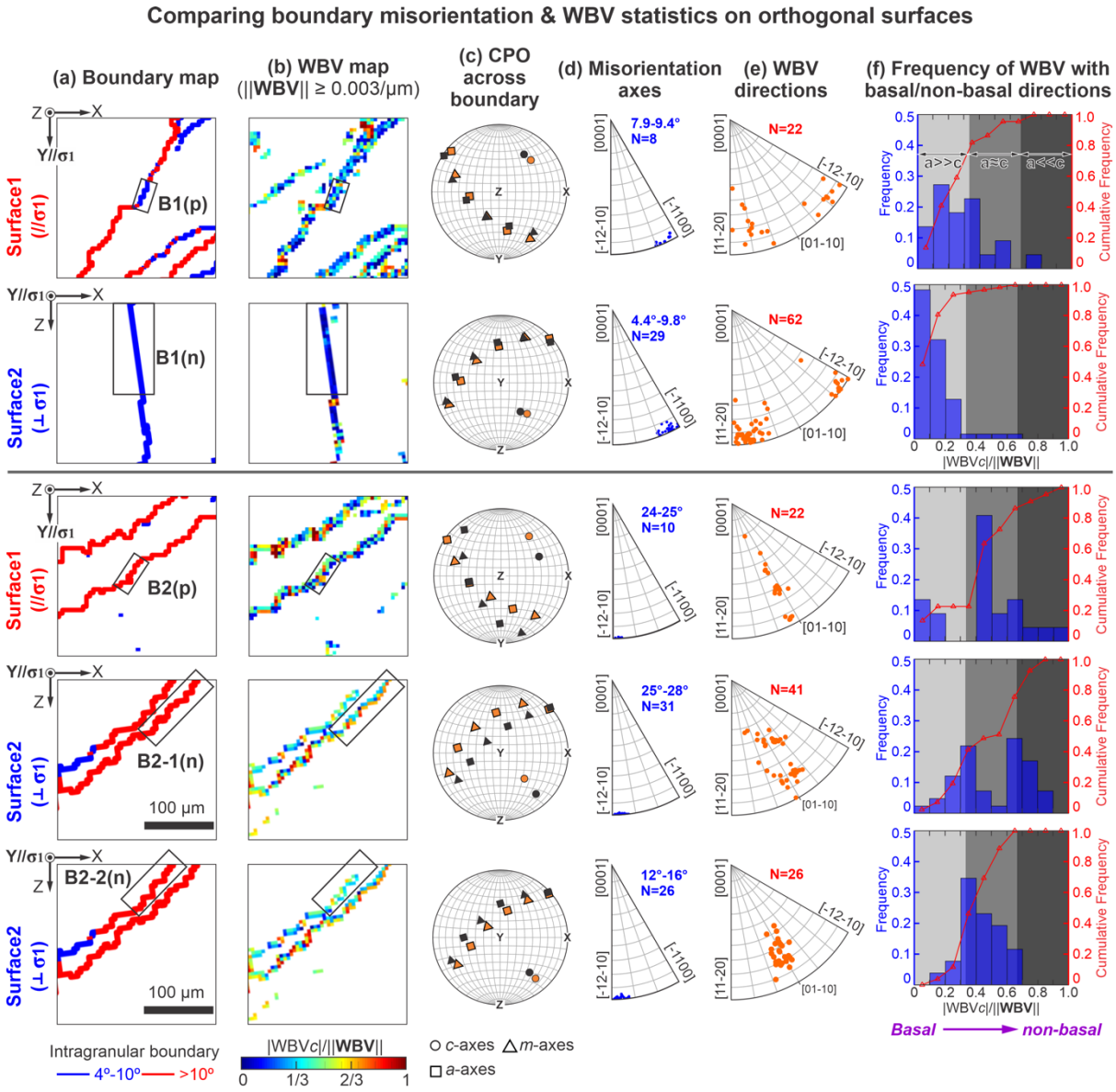

Figure 5. Comparing misorientation and WBV statistics across two sets of intragranular boundaries captured on orthogonal surfaces, corresponding to Fig. 4(d). (a) Intragranular boundary map with boundary segments coloured by their misorientation angles. (b) WBV map. Pixels with WBV greater than 0.003 μm^{-1} are coloured by their corresponding proportion of $<c>$-component WBV (ϕWBVc). The black box illustrates the region selected for crystallographic preferred orientation (CPO), misorientation, and WBV analyses. (c) CPO across each intragranular boundary. (d) Misorientation axes of each intra-

granular boundary with their directions displayed in inverse pole figure (IPF). (e) WBV directions across each intragranular boundary with their directions displayed in inverse pole figure (IPF). (f) The number frequency and cumulative number frequency distribution of ϕWBVc across each intragranular boundary.

4 Geometries of individual intragranular boundaries

To understand the processes by which intragranular boundaries form during deformation, we perform boundary trace analyses using geometric constraints from misorientation and WBV measurements (Sect. 2.3). Figures 6-10 are displayed in the same systematic format, reflecting our generic methodology. Our data concern the geometry of intragranular boundaries, and our aim is to understand the development of boundaries. In each figure we show:

(a) Two overview maps of intragranular boundaries.

(b) Maps that provide details of

- Misorientation angle along specific intragranular boundaries.
- Misorientation axes along specific intragranular boundaries.
- The ratio of $<c>$-component WBV magnitude relative to the total WBV magnitude, ϕWBVc (**WBVc/WBV**), along specific intragranular boundaries.

(c) Misorientation angle plotted against position measured along the boundary—augmenting the graphic in (b).

(d) Statistics of misorientation axes and WBV—augmenting the graphic in (b).

(e) Boundary trace analysis, synthesising all our information to diagnose boundary type.

Analyses were performed on intragranular boundaries in representative grains, which included grains in relatively hard-slip orientations—with c-axes at ~30° and ~80° from the compression axis (Figs. 6, 7)—and relatively easy-slip orientations—with c-axes at ~45° from the compression axis (Figs. 8–10). Intragranular boundaries chosen for analysis were either straight or slightly curved (Figs. 6(a)–10(a)), for reasons outlined above. Many intragranular boundaries intersect grain boundaries at one or both ends (e.g., B3 in Fig. 6(a); B4, B5 in Fig. 7(a); B7 in Fig. 8(a); B8 in Fig. 8(a); B9, B10 in Fig. 10(a)), whilst others are not connected to any grain boundary (e.g., B6 in Fig. 7(a)). Within the representative grains, intragranular boundaries show three types of geometrical compositions, characterised by either (1) one dominant boundary (e.g., Fig. 6(a)), (2) groups of boundaries sub-parallel to one another (e.g., Figs. 7(a), 10(a)), and (3) groups of boundaries that crosscut each other (e.g., Figs. 8(a), 9(a)). Many of the intragranular boundaries are dominated

by a combination of both low-angle (4–10°) and high-angle (>10°) components (e.g., B3–B8; Figs.6(a, b)–9(a, b)). Some other intragranular boundaries are dominated by low-angle components (e.g., B9, B10; Figs.10(a, b)). The microstructural details of these intragranular boundaries are summarised in Table 1.

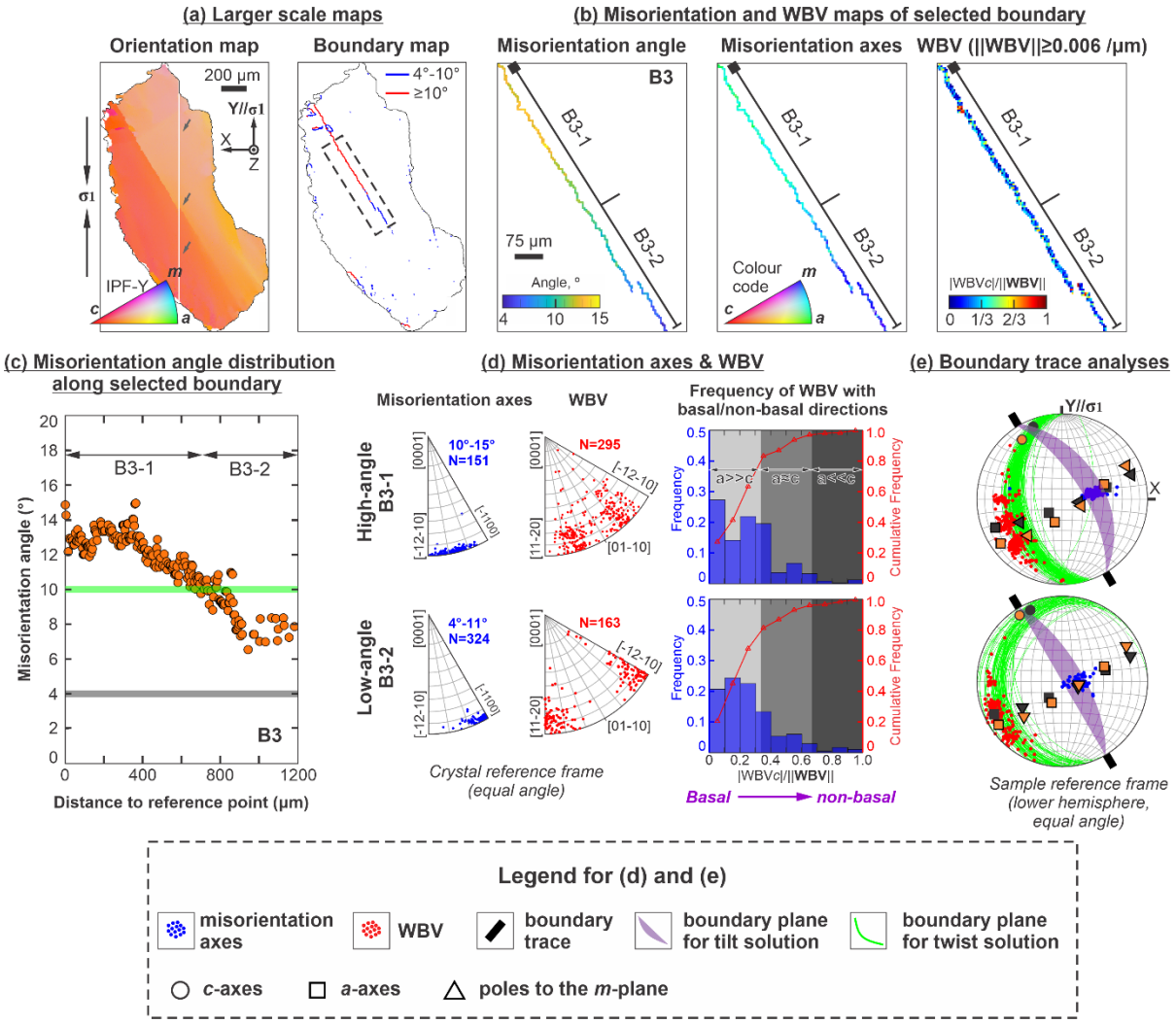

Figure 6. Misorientation and WBV analyses of intragranular boundaries developed within a typical grain from PIL275. (a) Orientation map and boundary misorientation angle map. Orientation maps are coloured by IPF-Y, which uses the colour map to indicate the crystallographic axes that are parallel to the vertical shortening direction (y-axis) as shown by the black arrow. Grey arrow points at eliminated repeated data points at stitches that are montage artefacts (Sect. 2.2). The black box illustrates the region selected for crystallographic

preferred orientation (CPO), misorientation, and WBV analyses. (b) Maps that display misorientation angle, misorientation axes, and ϕWBVc across individual intragranular boundary selected in (a). (c) Misorientation angle along individual intragranular boundary displayed in (b). (d) Misorientation axes and WBV directions across components within selected intragranular boundaries with their directions displayed in inverse pole figure (IPF). Bar plots show the number frequency and cumulative number frequency distribution of ϕWBVc across each intragranular boundary component. (e) Boundary trace analyses that include (1) directions of misorientation axes (blue dots) and WBVs (red dots), (2) boundary trace (heavy black bars stick out of primitive circle), (3) estimated range of tilt boundary plane (transparent purple sphere constrained by great circles), and (4) estimated twist boundary solution (thin green great circles that are perpendicular to misorientation axes).

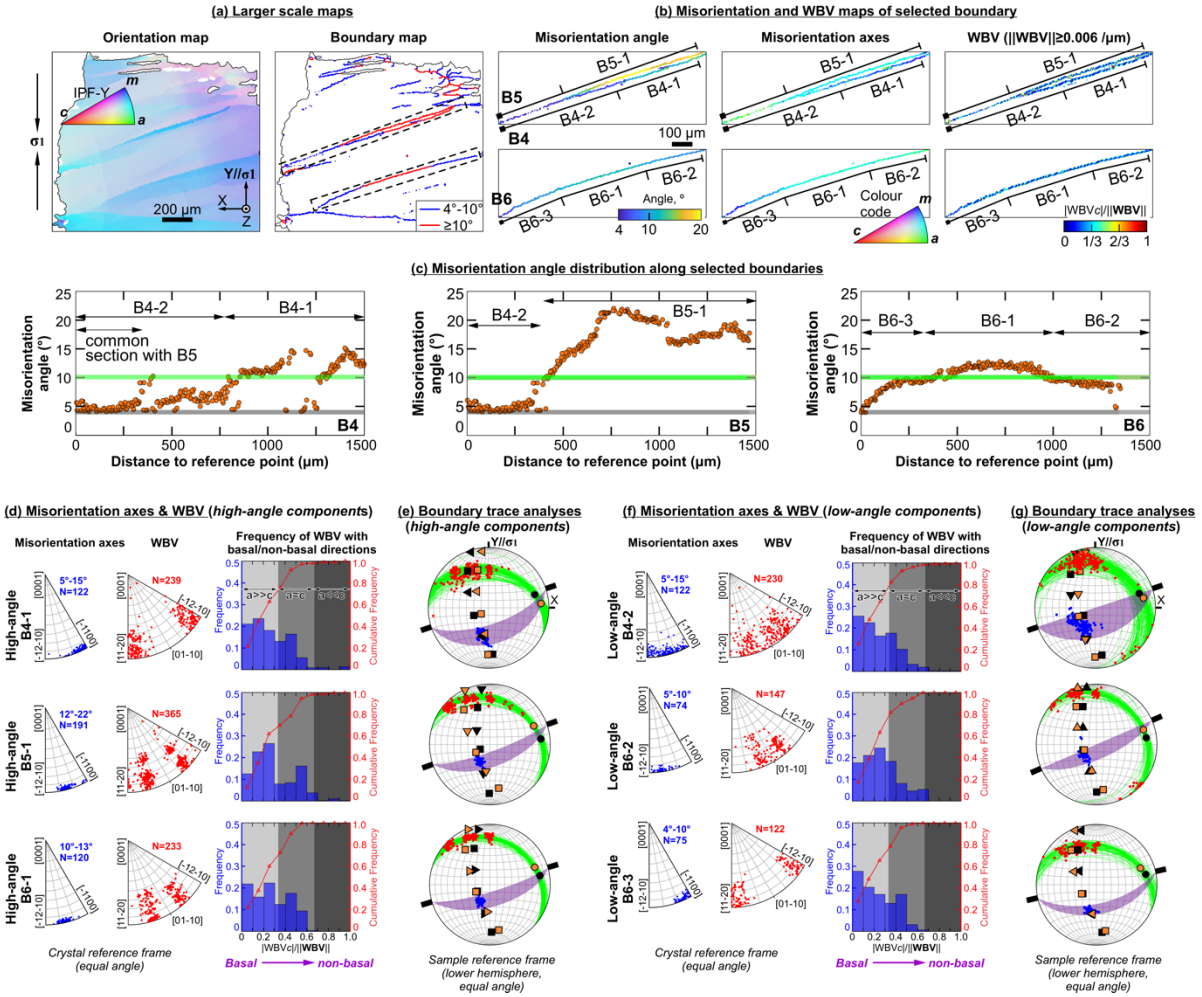

Figure 7. Misorientation and WBV analyses of intragranular boundaries developed within a typical grain from PIL271. Descriptions of (a) to (c) are the same as Figs. 6(a)–6(c). Descriptions of (d), (f) are the same as Fig. 6(d). Descriptions of (e), (g) are the same as Fig. 6(e).

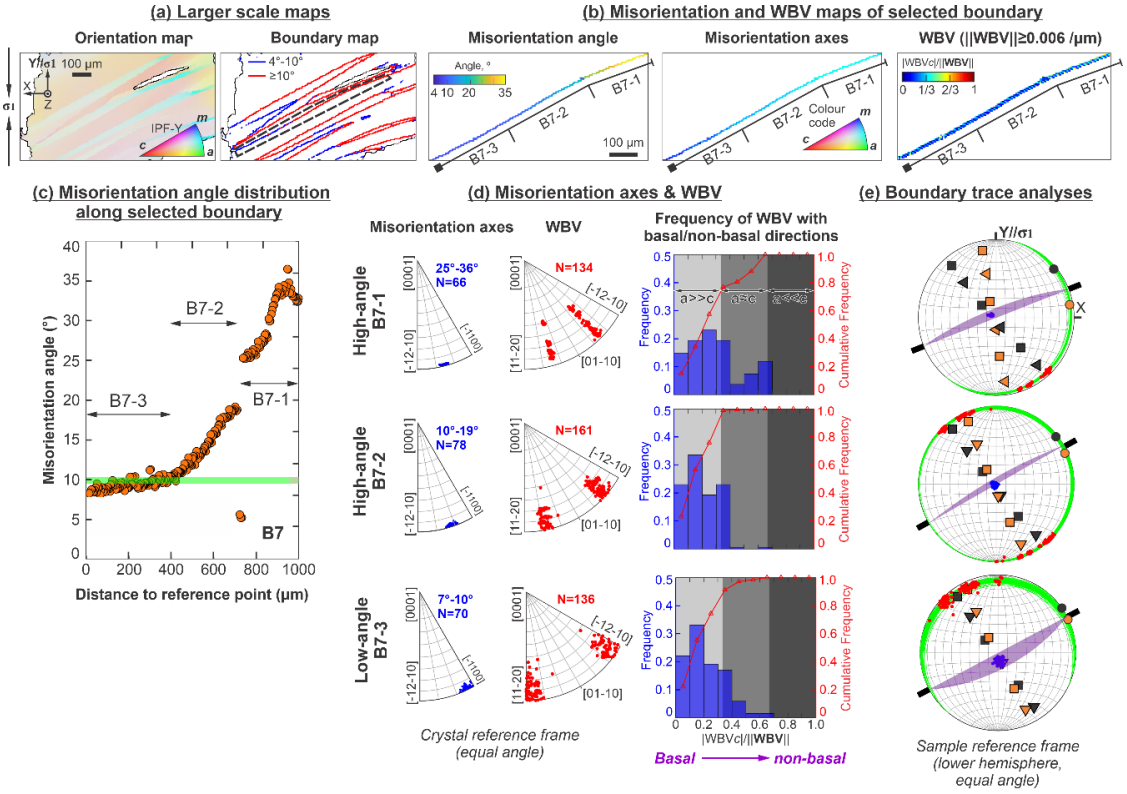

Figure 8. Misorientation and WBV analyses of intragranular boundaries developed within a typical grain from PIL275. Descriptions of (a) to (e) are the same as Figs. 6(a)–6(e).

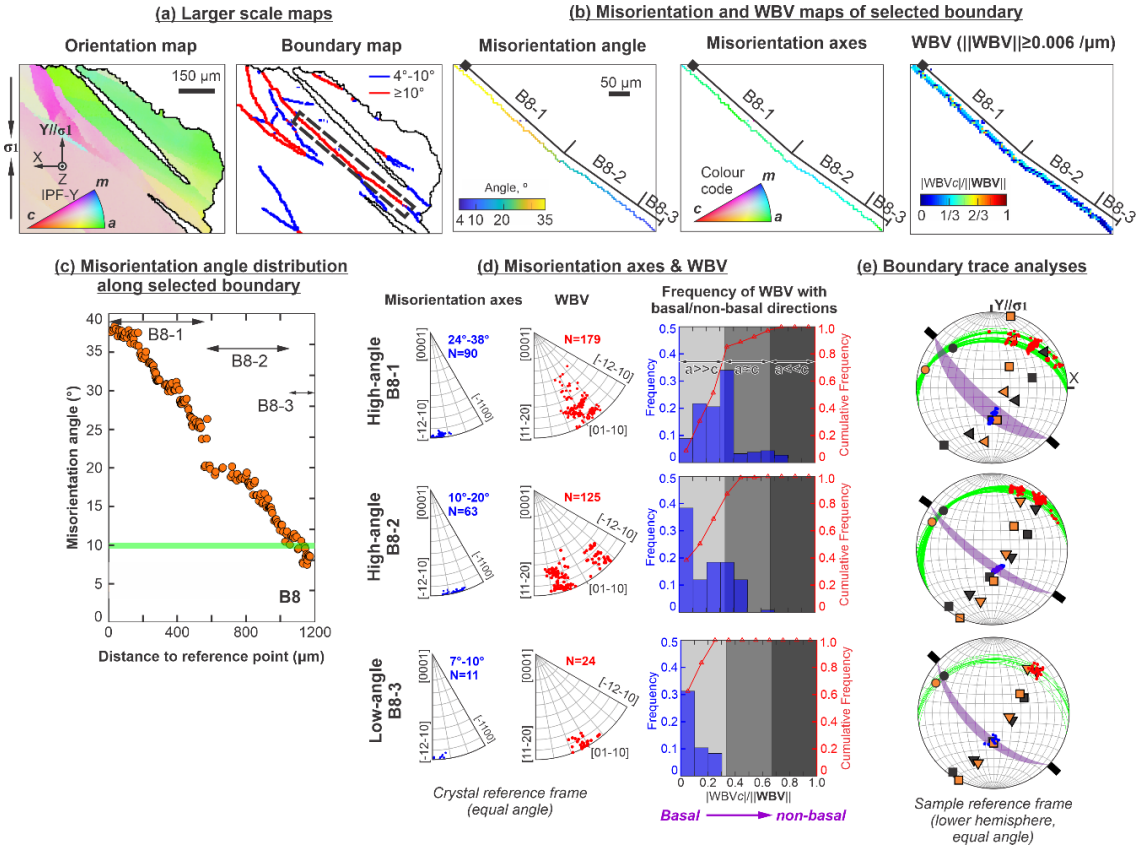

Figure 9. Misorientation and WBV analyses of intragranular boundaries developed within a typical grain from PIL271. Descriptions of (a) to (e) are the same as Figs. 6(a)–6(e).

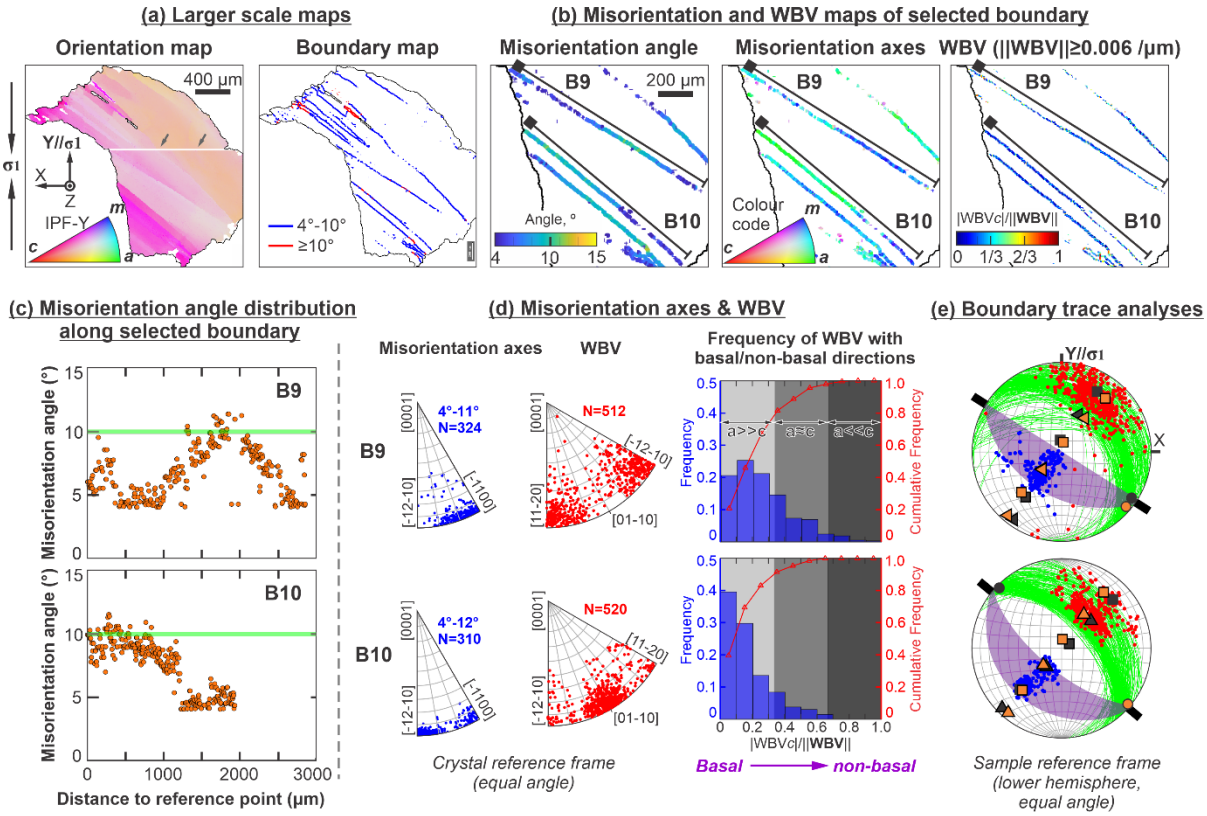

Figure 10. Misorientation and WBV analyses of intragranular boundaries developed within a typical grain from PIL275. Descriptions of (a) to (e) are the same as Figs. 6(a)–6(e).

Table 1. Summary of the intragranular boundary information from Figs. 6–10

Figure no.	Grain information	2-D intragranular boundary geometry	Misorientation angle variation along
	Sample no.	Angle between grain *c*-axes and $\sigma 1$	
6	PIL275	~30°	One dominant boundary
7	PIL271	~80°	Groups of boundaries sub-parallel t
8	PIL275	~45°	Groups of boundaries that crosscut
9	PIL271	~45°	Groups of boundaries that crosscut

Figure no.	Grain information	2-D intragranular boundary geometry	Misorientation angle variation alon
10	PIL275	~45°	Groups of boundaries sub-parallel t

4.1 Misorientation angle and misorientation axes

More than 50% of the all the intragranular boundaries within the entire EBSD map have misorientation angles higher than 6–8° (Fig. 2(c)). Misorientation angle changes smoothly and continuously along some of the selected intragranular boundaries (B3–B6, B9, B10; Figs. 6(b, c), 7(b, c), 10(b, c)), whereas other intragranular boundaries show a sudden change (5° within ~ 50 µm) of misorientation angle between low- and high-angle components (B7, B8; Figs. 8(b, c)–9(b, c)). Boundaries containing high-angle segments exhibit misorientation angles up to 38° (Figs. 9(a–c)).

The selected intragranular boundaries have misorientation axes lying mostly within 10° of the ice basal plane (B3–B10; Figs. 6(d), 7(d, f), 8(d)–10(d)). Many of the individual boundary components have misorientation axes clustering close to rational crystallographic axes within the ice basal plane (e.g., B3-2 in Fig. 6(d, e); B4-1, B5-1, B6-1, B6-3 in Fig. 7(d, f, g); B7-1, B7-2, B7-3 in Fig. 8(d, e); B8-1, B8-3 in Fig. 9(d, e)). Some other boundary components have misorientation axes that span a range of basal plane orientations between a[11-20] and m[10-10] (e.g., B3-1 in Fig. 6(d, e); B4-2, B6-2 in Fig. 7(d, f, g); B8-2 in Fig. 9(d, e); B9, B10 in Fig. 10(d, g)). For most of the selected individual intragranular boundaries, the low-angle and high-angle components have distinct misorientation axis orientations, but they mostly all lie within or very close to the ice basal plane (Figs. 6(d), 7(d, f), 8(d), 9(d)).

4.2 Weighted Burgers vectors

For most of the selected individual intragranular boundaries, the low-angle and high-angle components have distinct WBV orientations, albeit orientations mostly confined to the ice basal plane (Figs. 6(d), 7(d, f), 8(d), 9(d)). Thus, most (~60%) WBVs have ϕWBVc (WBVc/**WBV**) values <1/3, indicating a predominance of Burgers vectors lying within the ice basal plane (Figs. 6(d), 7(d, f), 8(d)–10(d)). However, high-angle boundary segments have WBVs that are much more dispersed into non-basal orientations than low-angle boundary segments, which mostly exhibit basal WBVs (Figs. 6(d), 7(d, f), 8(d)–10(d)). Consequently, WBV directions become dispersed along great-circle trajectories towards the <c>-direction in pole figures (Figs. 6(e), 7(e, g), 8(e)–10(e)).

4.3 Boundary trace analyses

Pole figures show that, WBVs (red dots) across all the selected intragranular boundaries have a smearing of orientations that are generally at 90° to misorientation axes (blue dots)—they lie within or very close to the planes that are perpendicular to misorientation axes (green great circles) (Figs. 6(e), 7(e, g), 8(e)–10(e)). The smearing WBVs can extend up to 40–90° along the planes normal to misorientation axes, and in most cases WBVs comprise distinct clusters (Figs. 6(e), 7(e, g), 8(e)–10(e)).

To examine whether each intragranular boundary more closely represents a pure-tilt or pure-twist boundary end-member, we estimated (1) the boundary planes for a twist boundary solution (green great circles in Figs. 6(e), 7(e, g), 8(e)–10(e)), where the boundary plane lies normal to its misorientation axes, and (2) the boundary planes for a tilt boundary solution (transparent purple sphere constrained by great circles), which contains the measured 2-D boundary trace (thick black bars extended outwards from the primitive circle) and the misorientation axes (blue dots) (Figs. 6(e), 7(e, g), 8(e)–10(e)). Each boundary can be fit with a tilt solution and a twist solution. However, the most likely solution is the one that predicts a boundary trace close to the observed boundary trace. For most of the selected intragranular boundary components, the planes for a twist boundary solution are 10–40° away from the measured 2-D boundary trace (B3 in Fig. 6(e); B4–B6 in Figs. 7(e, g); B8 in Fig. 9(e)). For the other boundary components, the planes for a twist boundary solution generally coincide with or within 10° to the measured 2-D boundary trace (B7 in Fig. 8(e); B9, B10 in Fig. 10(e)).

5 Discussion

5.1 Heterogeneous intragranular distribution of dislocations

For all the selected intragranular boundaries, the boundary misorientation axes and WBV across these boundaries have directions that are mostly clustering at rational crystallographic axes (Sect. 4.1), which are within or very close to the ice basal plane (Figs. 6–10; Sect. 3). The alignment of WBV and/or misorientation axes near rational crystallographic axes are geometrically consistent with the dislocation model—a model in which boundaries are composed of dislocations with rational Burgers vectors (Faul, 2021; Linckens et al., 2016; Piazolo et al., 2015; Weikusat et al., 2017; Wheeler et al., 2009). WBVs across all selected intragranular boundaries have directions that are at 90° to misorientation axes (Sect. 4.3; Figs. 6(e), 7(e, g), 8(e)–10(e)), indicating that Burgers vectors lie sub-perpendicular to the rotation (misorientation) axes, as expected for the hexagonal crystal symmetry of ice (Hondoh, 2000; Nabarro, 1967).

Intragranular boundaries rarely exhibit a uniform misorientation angle along their length. Instead, misorientation angle changes both gradually and sharply,

linking low- and high-angle segments (Sect. 4.1; Figs., 6(c)–10(c)), suggesting that dislocations are heterogeneously distributed within grains. We suggest that this heterogeneous distribution of dislocations reflects the relatively fast rate of deformation, compared to the rate of dislocation recovery, which ought to be relatively sluggish at the relatively cold conditions of these experiments.

The heterogeneous distribution of dislocations indicates grain-scale strain heterogeneity, which can contribute to strain weakening and, thereby, the formation of narrow localised shear zones (Bestmann & Prior, 2003; Hansen et al., 2016; de Riese et al., 2019; Wheeler et al., 2003). For example, strain energy differences promote dynamic recovery of dislocations and lead to the formation of intragranular boundaries. Subsequently, the enclosure and continuous rotation of intragranular boundaries—subgrain rotation recrystallization—can lead to the production of new, strain-free recrystallized grains (Jacka & Li, 2000; Urai et al., 1986; White, 1976). Moreover, the difference in the density of free dislocations between neighbouring grains might favour the migration of grain boundaries from the side with lower dislocation densities into the side with higher dislocation densities—strain-induced grain boundary migration (GBM) (Hirth & Tullis, 1992; Tullis & Yund, 1985). Thus, strain heterogeneity promotes dynamic recovery and recrystallization processes that reduce total strain energy. We expect strain weakening also at high temperature and low stress where strain heterogeneity might not be as significant. In addition, recovery and recrystallization commonly produce grain size reduction, which can then promote grain-size-sensitive, self-softening creep processes such as grain boundary sliding (De Bresser et al., 2001; Carlton & Ferreira, 2007; Hansen et al., 2011; Sheinerman et al., 2020).

5.2 The dislocation make-up of intragranular boundaries

Most of the selected intragranular boundaries—i.e., B3 in Fig. 6(e); B4–B6 in Figs. 7(e, g); B8 in Fig. 9(e)—have traces of the estimated twist boundary planes at relatively high angles (10–40°) to observed boundary traces (Sect. 4.3). These boundaries are unlikely to be twist boundaries and are therefore more likely to be tilt boundaries, comprised predominately of edge dislocations (Sect. 1). WBVs across these boundaries generally form distinct clusters within the ice basal plane (dominated by $<a>$-component) that often smear towards non-basal directions (dominated by $<a+c>$- and/or $<c>$-components) (Sect. 4.2; Figs. 6(d, e), 7(d–g), 8(d, e)–10(d, e)) as previous observed (Chauve et al., 2017; Piazolo et al., 2015). Moreover, the proportion of WBVs with non-basal directions is not negligible (~40%) (Sect. 4.2; Figs. 6(d), 7(d, f), 8(d)–10(d)). Thus, both basal and non-basal edge dislocations contribute to the development of the tilt boundaries examined here.

Only a few boundaries have traces consistent with a twist solution (Sect. 4.3; B7 in Fig. 8(e); B9, B10 in Fig. 10(e)). However, in each of these cases the tilt solution also provides a very similar boundary trace. Thus, we cannot easily determine a specific boundary type. If these boundaries are pure tilt bound-

aries, they reflect the recovery of both basal and non-basal edge dislocations, as discussed in the previous paragraph. If, on the other hand, these boundaries are pure twist boundaries, they should (due to geometrical constraints) relate to the recovery of dislocations with at least two distinct Burgers vectors (see Fig. 1(c, d)). Notably, WBVs for these boundaries typically cluster around one direction (within the ice basal plane—see B7 in Fig. 8(e); B9, B10 in Fig. 10(e)). As such, these boundaries are difficult to reconcile with a twist boundary model that requires Burgers vectors with at least two distinct directions. However, if these boundaries were pure twist boundaries, then the absence of additional WBV clusters may reflect a stereological bias, particularly since dislocation lines lying within (or close to) the sample surface produce minimal lattice distortion and are therefore difficult to detect—as mentioned above, the WBV method is weighted towards dislocation lines at high angles to the analysed surface. Boundaries comprised of mixed edge and screw dislocations are theoretically possible (Foreman, 1955; Peach & Koehler, 1950; Weertman, 1965), but have been rarely reported in any material (Konishi et al., 2020). Overall, intragranular boundaries in our samples appear to be dominated by basal and non-basal edge dislocations, but boundaries comprised of basal and non-basal screw dislocations may also be present. Our observation of a widespread non-basal edge dislocations is also consistent with Goldsby & Kohlstedt (2002), which suggests strain cannot solely be accommodated by basal dislocations alone. This hypothesis is consistent with the von Mises' criterion (von Mises, 1928)—five independent slip systems are required for a polycrystalline material to flow for any arbitrary homogeneous strain; four independent slip systems are required is the strain is inhomogeneous; three independent slip systems are required if dislocation climb is active, and possibly fewer still if diffusion creep and GBS are active (Goldsby & Kohlstedt, 2002).

Dislocation creep in ice is often thought to be rate-limited by the glide of non-basal edge dislocations (Castelnau et al., 2008; Duval et al., 1983; Goldsby & Kohlstedt, 2001). For example, Duval and others (1983) shows that, for ice single crystals, dislocation glide on the ice basal plane is at least 60 times easier than dislocation glide on non-basal planes. Thus, a significant increase in the proportion of non-basal dislocations should lead to strain hardening. However, the ice samples examined here underwent strain weakening with increasing strain (see Fan, Prior, Hager, et al., 2021). Strain weakening may be accounted for by (1) the alignment of ice basal planes into easy-slip orientations, and/or (2) widespread recovery and recrystallization, acting to relax strain heterogeneities, minimize dislocation tangles, and produce soft, (initially) strain-free recrystallized grains. In particular, strain-induced GBM is rapid at temperatures close to the ice melting point, and can promote strain weakening via the growth of grains in easy-slip orientations (Fan, Cross, et al., 2021). Therefore, any mechanical hardening associated with non-basal dislocations will likely be counteracted by strain-weakening processes, including crystallographic preferred orientation development and dynamic recrystallization.

5.3 Kinematic models for intragranular boundary development

Most of the analysed intragranular boundaries have both low-angle and high-angle components (Sect. 4.1; Figs. 6(b)–9(b)). Even though low- and high-angle components were segregated by an imposed arbitrary threshold angle—10° here, as is commonly used for minerals—they nevertheless exhibit distinct orientations of misorientation axes and WBV directions (Sects. 4.1, 4.2; Figs. 6(d), 7(d, f), 8(d), 9(d)). Thus, low- and high-angle intragranular boundary segments appear to have distinct crystallographic structures and may therefore form via different processes. Previous studies provide two kinematic models to explain the formation intragranular boundaries comprising components with both low- and high-angle segments:

(1) "Accumulation model" (Fig. 11(a)), which suggests that low-angle boundaries exert a greater attractive force on free dislocations than high-angle boundaries (Kapoor & Verdhan, 2016). Consequently, misorientation across pre-existing low-angle boundaries will increase as deformation progresses (Wang et al., 2020). Crucially, this model also implies that the length of a given intragranular boundary will not change significantly with increasing strain/time.

(2) "Propagation model" (Fig. 11(b)), which suggests that dislocations will more easily pile up in front of intragranular boundaries with relatively large misorientation angles (Hu et al., 2018). Consequently, high-angle intragranular boundaries can propagate (and growth in length) more effectively as they become more mobile during deformation. This model also implies that the intragranular boundaries should become longer with increasing strain/time.

However, neither model provides a mechanism by which misorientation axes and slip directions can change during boundary rotation (as in the "accumulation" model) and/or propagation (as in the "propagation" model). To undergo a change in misorientation axis and/or slip direction during boundary rotation or propagation, boundaries must change their geometry—that is, become more curved or irregular with increasing strain/time. Yet the boundaries analysed in this study, which are mostly planar, are comprised of several crystallographically-distinct segments, each with a different WBV direction and misorientation axis (Sect. 2.3). To account for this observation, we propose a new kinematic model for intragranular boundary development:

(3) "Intersection model" (Fig. 11(c)), whereby an intragranular boundary can develop through the accretion of individual boundary segments, each with a distinct WBV direction and misorientation axis. Intragranular boundary segments can therefore form by rotations around distinct misorientation axes. These separately formed intragranular boundary segments intersect after or during their formation. The operation of "intersection model" requires the length of intragranular boundary becomes longer with increasing strain/time.

Intuitively, it might require more energy to form and intersect multiple isolated

boundary segments (each with a distinct crystallographic geometry) than, for example, propagate a single pre-existing low-angle boundary. We speculate that high differential stresses, as experienced by the ice samples deformed in this study, might favour the boundary intersection model proposed here. However, we should note that our current data sets are insufficient to provide more information on the evolution of boundary crystallographic geometry after the connection of individual intragranular boundaries. Acquiring the evolution of boundary crystallographic geometry would require quantitative *in situ* data—from, for example, EBSD (Piazolo et al., 2004; Tokita et al., 2017), synchrotron diffraction (Cornelius & Thomas, 2018), or neutron diffraction (Nervo et al., 2016)—to examine how boundary geometry and structure change over time.

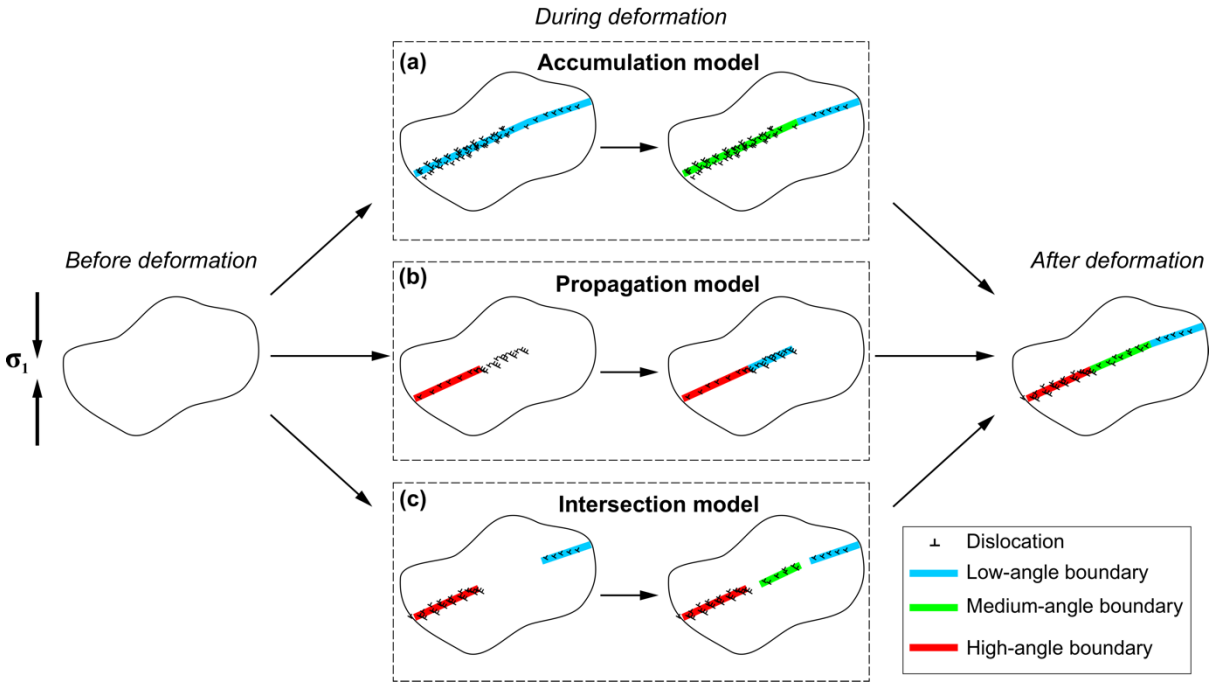

Figure 11. Illustration of possible intragranular boundary development kinematic models that can lead to the formation of identical boundaries composed by low-, medium- and high-angle components after deformation. Black non-vertical arrows indicate the sequence of intragranular boundary development. The kinematic models include (a) "accumulation model", (b) "propagation model", and (c) "intersection model".

5.4 Crystallographic control of grain and intragrain boundary structure

In the samples examined here, intragranular boundaries commonly develop misorientation angles up to ~20°—and up to 38° in extreme cases—while maintain-

ing a strong crystallographic control; that is, while maintaining misorientation axes and WBV directions clustered around rational crystallographic axes (Sect. 4.1; e.g., B8-1, B8-2 in Figs. 9(c), (d)). Furthermore, both low- and high-angle intragranular boundary segments have misorientation axes and WBVs that are typically confined to the ice basal plane (Sects. 4.1, 4.2; Figs. 6(d), 7(d, f), 8(d)–10(d)). Together, these observations suggest that intragranular boundary structure is strongly crystallographically controlled, even at large misorientation angles (» 10°) where boundaries are typically thought to be highly disordered.

To investigate whether grain boundaries are similarly crystallographically controlled, we compare the misorientation axis distribution of intragrain and grain boundaries in Fig. 12. Boundaries are grouped into bins based on their misorientation angle, with a 5° bin width, to see whether boundary structure changes with increasing misorientation. Only boundaries with misorientation angles up to 30° are analysed, since there are very few intragranular boundaries with misorientation angles >30°. As shown in Fig. 12, intragranular boundaries and grain boundaries have fundamentally different misorientation axis distributions, regardless of misorientation angle. For intragranular boundaries, misorientation axes lie mostly within the ice basal plane, becoming clustered more strongly around the a[11-20] direction as misorientation angle increases (Fig. 12). For grain boundaries, on the other hand, misorientation axes are much more randomly oriented, showing only a weak clustering near the ice basal plane (Fig. 12). Similar observations have been reported for ice samples deformed under a wider range of temperatures (-10 to -30°C) (Fan et al., 2020). Such observations suggest that subgrain rotation—which continuously increases the misorientation angle across intragranular boundaries—cannot solely modify the crystallographic structure of intragrain or grain boundaries, since intragranular boundaries maintain a strong preferred misorientation axis to large misorientation angles. This finding contradicts previous assertions that subgrain rotation can randomise the orientations of recrystallized grains during deformation (Lopez-Sanchez et al., 2021). We suggest, instead, that grain boundary formation—that is, the enclosure a crystallographically-continuous region by a high-angle boundary—is necessary for the weakening of a pre-existing CPO (and, necessarily, the associated misorientation axis distribution of a polycrystal). This is because grain boundary formation can allow other deformation mechanisms, namely, grain boundary sliding, to operate and produce relative grain rotations (Goldsby & Kohlstedt, 1997). Alternatively, spontaneous nucleation (i.e., the nucleation of grains in random orientations; (Herwegh & Handy, 1996) may produce recrystallized grains with orientations that are independent from original remnant grains. This process would produce a similarly weak or random misorientation axis distribution. However, given that grain boundary misorientation axes cluster around the ice basal plane (albeit weakly), as observed for intragranular boundaries, we find it more plausible that the misorientation axis distribution is progressively weakened following grain boundary formation, for example via grain boundary sliding.

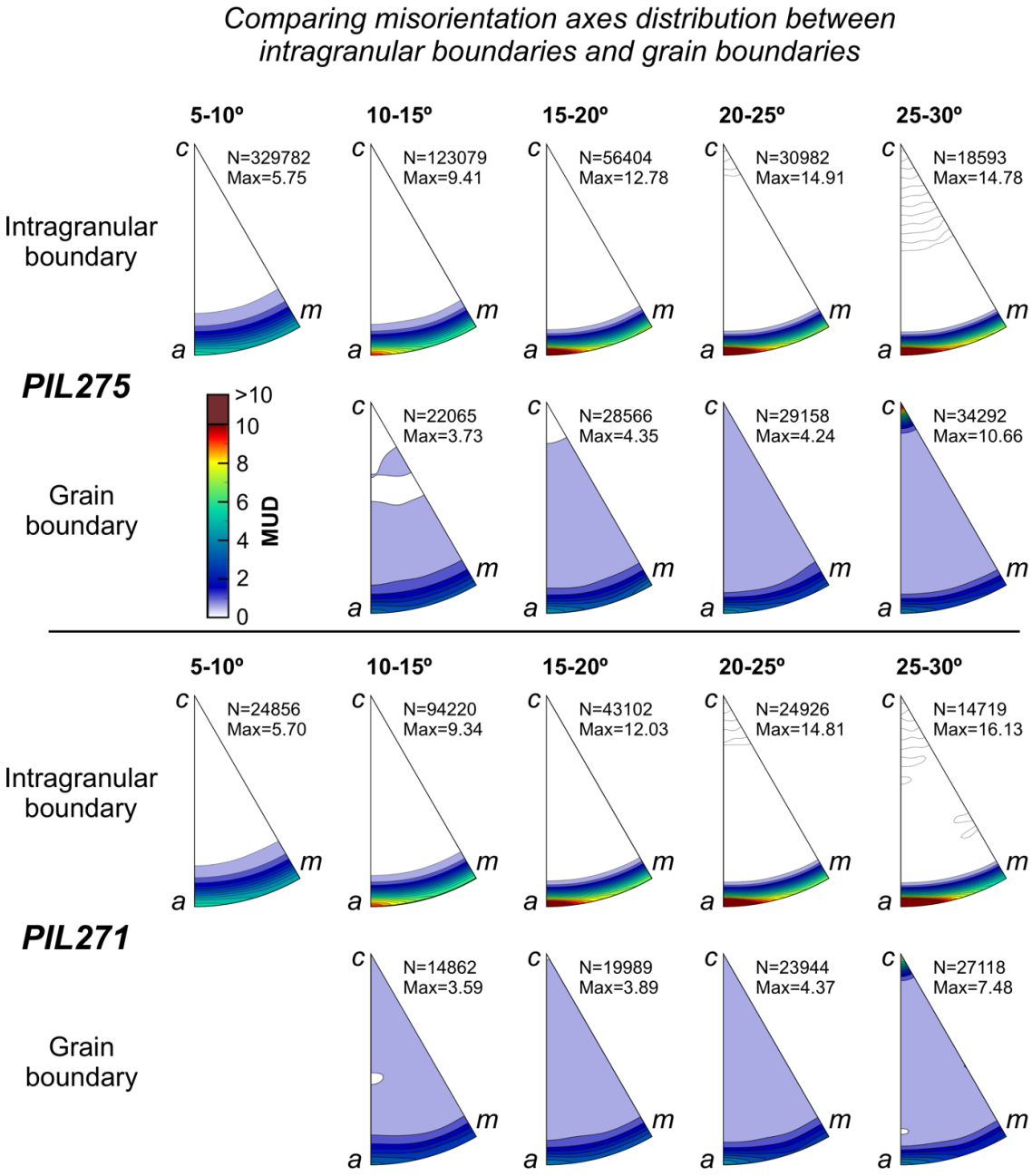

Figure 12. Comparing the misorientation axes distribution with a misorientation angle interval of 5° between intragranular boundaries and grain boundaries of recrystallized grains. The EBSD data set and details for the segregation of recrystallized grains are provided in Fan, Prior, Hager, et al., (2021). The misorientaion axes distributions are displayed as contoured inverse pole figures

(IPFs), with the number of boundary elements (N) and the maximum MUD value (Max) provided at the top right corner.

5.5 Misorientation angle threshold for the transition of ice intragranular boundary into grain boundary

As dislocations are continuously stacked into an intragranular boundary, misorientation across the boundary will progressively increase (Bell et al., 1986). However, there is a limit to the number (or, rather, density) of dislocations that can be added to an intragranular boundary before its dislocation cores overlap, rapidly increasing the degree of grain boundary disorder (Hirth & Balluffi, 1973; Li, 1961; Read & Shockley, 1950). Therefore, it is common to impose a threshold angle to separate intragranular boundaries from grain boundaries. For minerals other than ice, transmission electron microscopy (TEM) has often been used to quantify the threshold misorientation angle above which lattice fringes (representing regular arrays of dislocations) become weak and difficult to distinguish (Heinemann et al., 2005; McLaren, 1991; Shigematsu et al., 2006). Such studies have found that grain boundaries are characterized by a misorientation angle threshold of 9–14° in quartz (Shigematsu et al., 2006), 9.9–21.5° in olivine (Heinemann et al., 2005), and ~15° in feldspars (McLaren, 1991). Unfortunately, TEM is extremely challenging for ice (Baker, 1997, 2002, 2003) and has not, to date, been used to understand differences between intragranular boundaries and grain boundaries in ice. In lieu of TEM data, here we rely on our new EBSD data to constrain the grain boundary misorientation angle threshold for ice.

Our data show that most intragranular boundaries ($> 50\%$) have misorientation angles greater than ~6–8° (Fig. 2(c); Sect. 4.1), suggesting that the threshold angle should be greater than 5–7°, as previously used (Chauve et al., 2017; Weikusat et al., 2017). We apply neighbour-pair and random-pair misorientation statistics to place an upper limit on the grain boundary threshold angle. Specifically, we plot the neighbour-pair misorientation angle distribution (blue bar) and random-pair misorientation angle distribution (red bar) using the whole EBSD data set for each sample (Fig. 2(d)). For all the deformed ice samples, the frequency of neighbour-pair and random-pair misorientation distributions intersect at misorientation angles between 10° and 30° (Fig. 1(e), this study; see also Figs 4(f)–6(f) in Fan et al., 2020). The difference between neighbour-pair and random-pair misorientation angle distribution can indicate adjacent grains are (1) physically interacted, and/or (2) inherited from a precursor microstructure—they all require the formation of grain boundary (Wheeler et al., 2001). After the formation of grain boundary, processes such as GBS and grain rotation can modify the grain boundary misorientation angle. Consequently, we suggest that grain boundaries form once a continuous region of crystal lattice becomes misoriented, with respect to its surrounding region, by an angle of 10–30°. This finding is consistent with our misorientation axis analyses (Fig. 12), which show that grain boundaries (defined in this study using an angle of 10°) are crystallographically distinct from intragranular boundaries.

Moreover, simple tests demonstrate that median grain sizes do not change significantly for threshold angles in the range 10–30° (Appendix A). In summary, we recommend using a grain boundary misorientation threshold angle of 10° for ice, at least until better (e.g., *in situ* or cryo-TEM) data become available.

6 Conclusions

1. To quantify the crystallographic structure of intragranular boundaries in deformed, coarse-grained ice polycrystals, we applied misorientation and weighted Burgers vector (WBV) analyses across planar intragranular boundaries formed during high-temperature (T_h= ~0.9), high stress (> 1 MPa) deformation. Misorientation angle along these boundaries changes both gradually and sharply, linking low- (< 10°) and high-angle (> 10°, up to 38°) segments. This observation suggests that intragranular dislocations are heterogeneously distributed, reflecting intragranular strain heterogeneity.

2. To constrain the types of dislocations contained within intragranular boundaries, we used boundary trace analyses to segregate boundaries into tilt (predominately edge dislocation) and twist (predominately screw dislocation) end-member categories. Most intragranular boundaries appear likely to be tilt boundaries, with WBVs generally clustering within the ice basal plane. However, a non-negligible proportion of WBVs deviate towards non-basal directions. Thus, mixed basal and non-basal edge dislocations facilitate the development of intragranular boundaries. Screw dislocations (i.e., twist boundaries) appear less common.

3. Planar intragranular boundaries are comprised of multiple segments, with both low- and high-angle misorientation angles, and distinct crystallographic structures (i.e., distinct misorientation axes and WBVs). Previous models for intragranular boundary development cannot explain the observed variations in boundary structure without significant bending of the boundary. Therefore, we propose a new model whereby intragranular boundaries form through the intersection of multiple, crystallographically-distinct boundary segments.

4. Misorientation axes of intragranular boundaries lie predominately within the ice basal plane, whereas the misorientation axes of grain boundaries are much more dispersed. Together, these observations suggest that subgrain rotation—which increases the misorientation angle across intragranular boundaries—is crystallographically controlled and does not (on its own) modify boundary misorientation axes. Instead, boundary misorientation axes become markedly randomized following grain boundary formation. We suggest that this randomization most likely arises from the activation of grain boundary sliding following dynamic recrystallization or probably from nucleation with random orientations.

5. Neighbour-pair and random-pair misorientation angle distributions intersect at misorientation angles between 10° and 30°. This intersection represents the misorientation angle at which neighbouring crystal lattices begin to interact

during deformation and places an upper limit of 10–30° on the misorientation angle threshold used to distinguish grain boundaries from intragrain boundaries. We recommend using a threshold angle of 10° for ice, based on the above observations of misorientation axis randomisation across grain boundaries defined using an angle of 10°.

6. Ice is often considered an analogue for rock-forming minerals such as quartz and olivine (Wilson et al., 2014). Thus, in closing, we suggest that these findings may apply more broadly to other rock-forming minerals, particularly those deformed under high homologous temperatures (T_h= ~0.9), as in this study.

Appendix A Testing the impact of grain boundary threshold angle on grain size statistics

We calculated the grain size statistics using previously published EBSD data collected from ice samples with an initial grain size of ~300 and 1300 µm (Fan et al., 2020; Fan, Prior, Hager, et al., 2021). These samples were deformed under uniaxial compression at temperatures between -10 and -30 °C with the true axial strain rate between ~1×10^{-5} and 6×10^{-5} s^{-1} (Table A1). The grain construction follows the procedure described in Sect. 2.2 using a grain boundary threshold angle of 5°, 7°, 10°, 20°, and 30°, and grain size statistics of lower quartile, medium, and higher quartile grain sizes were recorded (Table A1). In general, the median grain sizes at grain boundary threshold angles of 10–30° are very similar (Fig. A1). For individual samples, e.g., undeformed coarse-grained ice, the median grain size at grain boundary threshold angles of 10–30° is ~2 times of the median grain size at grain boundary threshold angles of 5–7° (Fig. A1).

Table A1. Comparing grain size statistics calculated with different grain boundary threshold angles

Sample no.	T (°C)	Final strain	Final stress (MPa)	Final strain rate (/s)	Grain size statistics (µm) at different grain boundary threshold angles (lower quartile/**median**/higher quartile)				
					°	°	°	°	°
Undeformed fine-grained	N/A		N/A	N/A	/**291**/413	/**291**/414	/**293**/414	/**298**/436	/**317**/466
PIL176				1.04E-05	/**112**/249	/**123**/254	/**127**/257	/**125**/260	/**129**/261
PIL177				1.21E-05	/**90**/149	/**92**/154	/**93**/156	/**93**/158	/**93**/161
PIL182				8.94E-06	/**118**/214	/**126**/224	/**130**/233	/**134**/246	/**128**/252
PIL255				1.28E-05	/**52**/76	/**53**/78	/**54**/82	/**57**/90	/**57**/91
PIL165				1.09E-05	/**93**/215	/**99**/223	/**106**/229	/**127**/253	/**141**/254
PIL268				1.31E-05	/**37**/53	/**39**/55	/**40**/59	/**42**/67	/**41**/62
Undeformed coarse-grained	N/A		N/A	N/A	/**535**/1338	/**811**/1501	/**1293**/1783	/**1368**/1799	/**1374**/1830
PIL275				1.20E-05	/**42**/65	/**47**/69	/**52**/76	/**53**/77	/**51**/75
PIL271				6.00E-05	/**41**/59	/**44**/61	/**47**/63	/**48**/64	/**48**/66

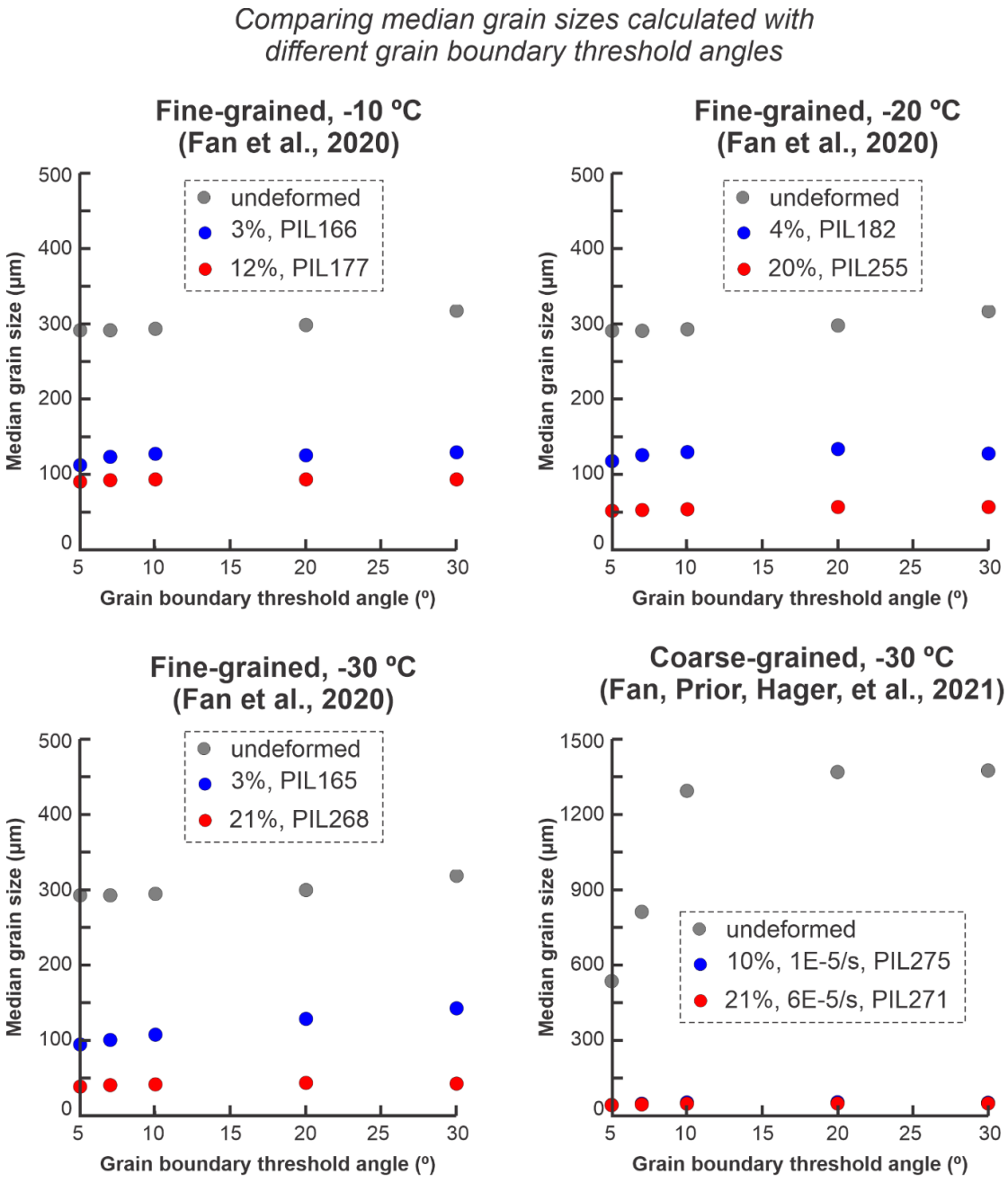

Figure A1. Comparing the median grain sizes calculated with different grain boundary threshold angles of 5°, 7°, 10°, 20°, and 30°. A complete data set has been provided in Table A1. The EBSD data used for calculation were provided in Fan et al. (2020) and Fan, Prior, Hager, et al. (2021).

Appendix B Details of sample fabrication and uniaxial compression experiments

B.1 Sample fabrication and deformation assembly

Ice seeds with particle sizes of 1.6–2 mm were packed into cylindrical moulds (25.4 mm inner diameter) at -30°C. We applied a "wet-sieve" method (Fan, Prior, Hager, et al., 2021)—pouring liquid nitrogen over crushed ice cubes (made from deionized ultra-pure water) while sieving—to remove unwanted fine ice seeds ($<$ 300µm) that are electrostatically clumped on target ice seeds (1.6–2 mm). After that, the packed moulds were flooded with degassed, deionized, ultra-pure water at 0°C under vacuum. The flooded moulds were then immediately placed vertically on a copper plate for 24 hours at −30°C with polystyrene insulating the cylinders from all the other sides. This step ensures that the freezing front migrates slowly upwards, minimizing the entrapment of bubbles within the samples.

Ice samples were gently pushed out from the moulds using an Arbor press after ~24 hours. Ice samples were cut and polished on both ends to limit their lengths to 1.5–2.0 times the sample diameter and to ensure that both ends were flat and perpendicular to the sample cylindrical axis. Each sample was encapsulated in a thin-walled indium jacket tube (~0.38 mm wall thickness) with the bottom already welded to a stainless-steel end-cap. The top of indium jacket tube was then welded to a steel semi-internal force gauge, with a zirconia spacer placed between the force gauge and sample to thermally insulate the sample during welding. During welding, each sample was kept submerged in a -60°C ethanol bath.

B.2 Experimental process

Ice samples were deformed under uniaxial compression in a cryogenic apparatus (Heard et al., 1990) under ~40 MPa of nitrogen gas confining pressure in the Ice Physics Laboratory, University of Pennsylvania. The ice samples were deformed at -30 °C under constant displacement rates, yielding true axial strain rates of $\sim 1 \times 10^{-5}$ (sample no. PIL275) and $6 \times 10^{-5} s^{-1}$ (sample no. PIL271). The experiments were terminated once the true axial strain reached ~10%, with the mechanical data (stress-strain and strain rate-strain curves) reported in (Fan, Prior, Hager, et al., 2021). After deformation, the samples were immediately extracted from the apparatus within 15 minutes, photographed and measured. Samples were progressively cooled to ~-30, -100 and -196 °C within ~15 minutes and eventually stored in a liquid nitrogen dewar.

Appendix C Details of EBSD data acquisition

Full crystallographic orientation data were collected from each ice sample using the cryogenic electron backscatter diffraction (cryo-EBSD) technique (Iliescu et

al., 2004). For each ice sample, a slice with the thickness of ~5 mm was extracted along the cylinder axis at -20°C within 5 minutes using a bandsaw. We acquired polished sample surfaces by hand lapping the ice slice, with one side frozen on a copper ingot, at -40°C on sandpapers with grit sizes of 80, 240, 600, 1200 and 2400. After polishing, ice-ingot assemblies were stored at liquid nitrogen temperature before being transferred to a scanning electron microscope (SEM) for cryo-EBSD data acquisition.

We collected EBSD data from the polished surface of each ice slice. A Zeiss Sigma VP FEG-SEM combined with an Oxford Instruments' Symmetry EBSD camera was used for the data collection. The ice-ingot assembly was transferred to a cold SEM stage maintained at ~-100°C. Pressure cycling in the SEM chamber was performed to remove frost and create a damage-free sample surface via sublimation (Prior et al., 2015). We acquired reconnaissance large-area EBSD maps with a step size of 5 µm at a stage temperature of ~-95°C, with 2–5 Pa nitrogen gas pressure, 30kV accelerating voltage and ~60 nA beam current. Large-area montage maps were constructed by stitching individual frames (EBSD maps) together, using the Oxford Instruments' Aztec software.

Appendix D Assessing the impact of EBSD data interpolation on misorientation and WBV statistics

We used sample PIL271 to assess the impact of EBSD data interpolation on the statistics of misorientation axes and WBVs. In practical, we collected EBSD data from the same surface area (rows 1, 3; Fig. A2) using (1) "speed 2" mode with a fast frame rate (maximum ~1500 Hz, 8x8 camera binning), and (2) resolution mode with a slow frame rate (maximum ~100 Hz, no camera binning). Moreover, we interpolated the EBSD data (details in Sect. 2.2) collected under "speed 2" mode (row 2; Fig. A2). We compared the misorientation and WBV statistics calculated from the same sub-area within (1) raw data collected under "speed 2" mode, (2) interpolated data collected under "speed 2" mode, and (3) raw data collected under "resolution" mode (Figs. A2, A3). We calculated misorientation axes and WBV direction distributions (displayed as IPFs) as well as ϕWBVc distribution (displayed as bar plots; Sect. 2.3.2) for the whole sub-area as well as individual intragranular boundaries identified within the sub-area (Fig. A3). The result shows, the pattern of misorientation axes and WBV distributions are generally very similar amongst raw EBSD data collected under fast and slow frame rates and interpolated EBSD data collected under fast frame rates (Fig. A3). This observation suggests the interpolation of EBSD data will introduce insignificant impact on misorientation and WBV statistics.

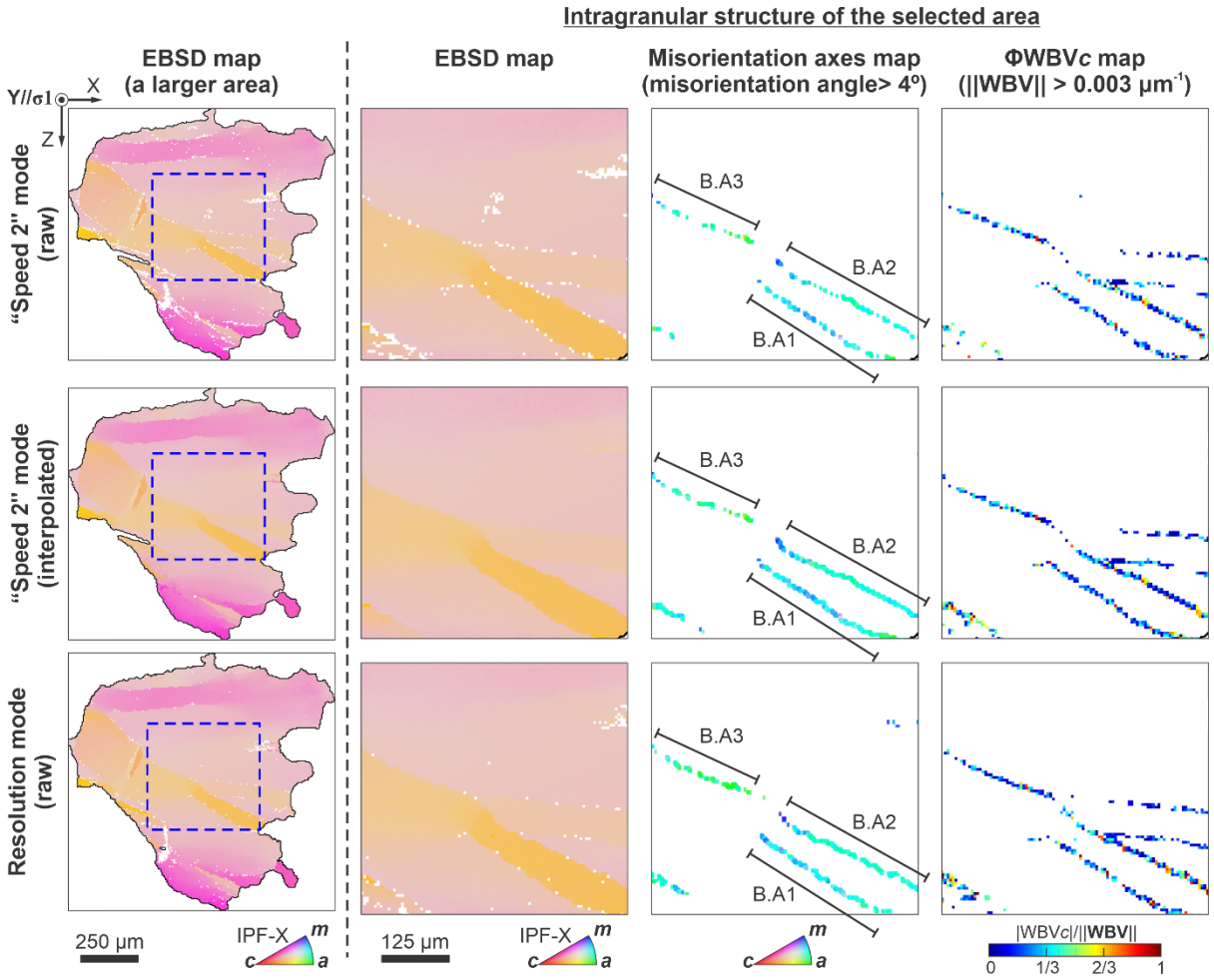

Figure A2. Comparing microstructural maps collected with different speed modes for EBSD data collection. The EBSD maps (columns 1, 2) are coloured by IPF-X to favour the identification of intragranular distortion. The first and third rows used raw, un-interpolated EBSD data collected under "speed 2" mode (maximum ~1500 Hz, 8x8 camera binning) and resolution mode (maximum ~100 Hz, no camera binning). The second row used interpolated EBSD data collected under "speed 2" mode. A selected sub-area (within blue rectangular in Column 1) was chosen for misorientation and WBV analyses (Columns 2–4).

Comparing misorientation and WBV statistics calculated from EBSD data collected with different speed modes

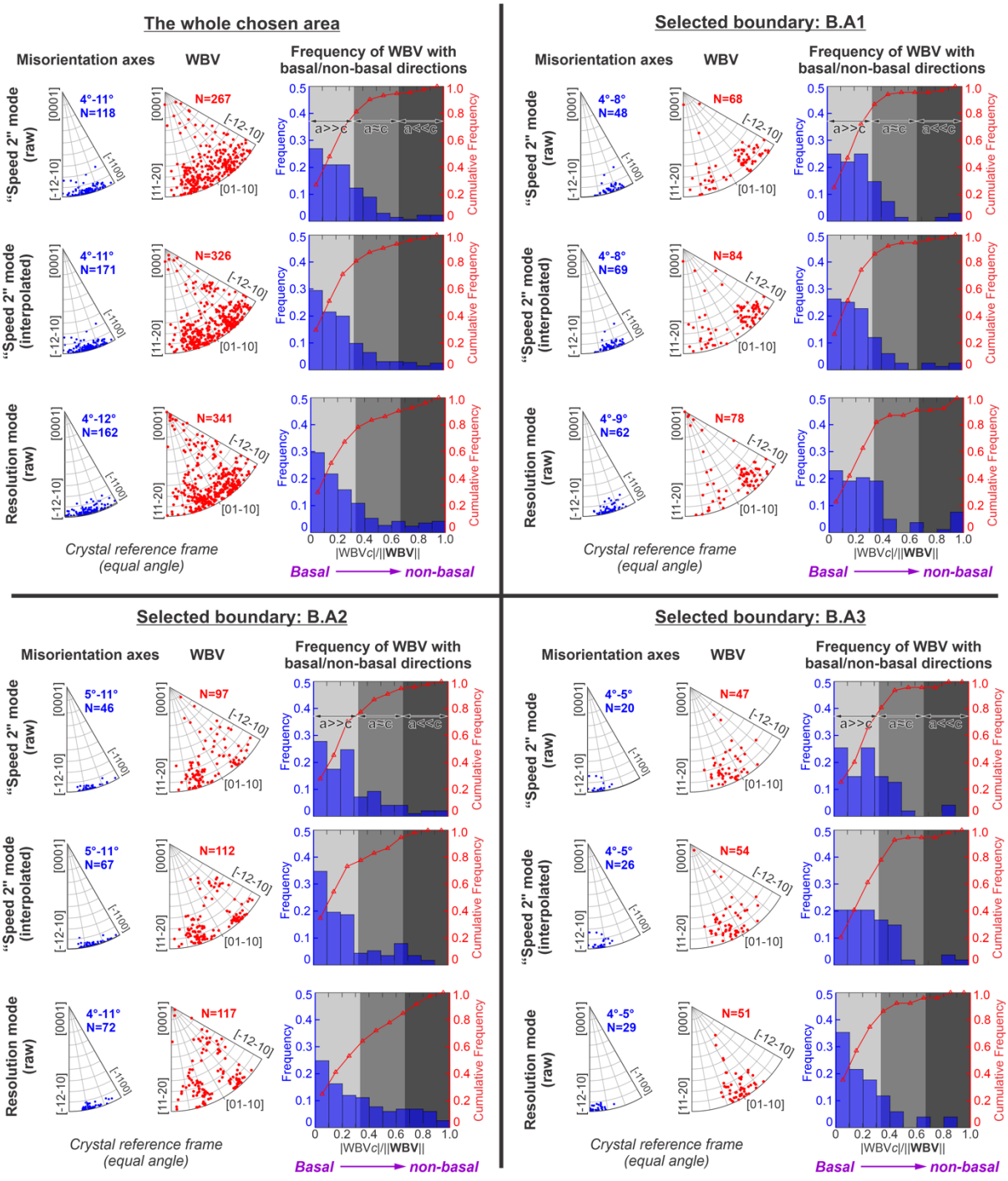

Figure A3. Comparing misorientation and WBV statistics for a selected area as well as individual intragranular boundaries displayed in Fig. A2. Misorientation axes and WBV directions were displayed in inverse pole figure (IPF). Bar plots show the number frequency and cumulative number frequency distribution of ϕWBVc (Sect. 2.3.2).

Data availability

Data can be obtained via Mendeley Data (https://doi.org/10.17632/tstn4krkt8.1; Fan et al., 2021).

Competing interests

The authors declare that they have no conflict of interest.

Acknowledgements

We are thankful to Pat Langhorne for providing the cold-room facility at University of Otago. This work was supported by a NASA fund (grant no. NNX15AM69G) to David L. Goldsby and two Marsden Funds of the Royal Society of New Zealand (grant nos. UOO1116, UOO052) to David J. Prior. Sheng Fan was supported by the University of Otago doctoral scholarship, the Antarctica New Zealand doctoral scholarship, a research grant from New Zealand Ministry of Business, Innovation and Employment through the Antarctic Science Platform (ANTA1801) (grant no. ASP-023-03), and a New Zealand Antarctic Research Institute (NZARI) Early Career Researcher Seed Grant (grant no. NZARI 2020-1-5).

References

Ashby, M. F. (1970). The deformation of plastically non-homogeneous materials. *Philosophical Magazine*, *21*(170), 399–424. https://doi.org/10.1080/14786437008238426Bachmann, F., Hielscher, R., & Schaeben, H. (2011). Grain detection from 2d and 3d EBSD data—Specification of the MTEX algorithm. *Ultramicroscopy*, *111*(12), 1720–1733. https://doi.org/10.1016/j.ultramic.2011.08.002Baker, I. (1997). Observation of dislocations in ice. *Journal of Physical Chemistry B*, *101*(32), 6158–6162. https://doi.org/10.1021/jp963211sBaker, I. (2002). Examination of Dislocations in Ice. *Crystal Growth and Design*, *2*(2), 127–134. https://doi.org/10.1021/cg0100282Baker, I. (2003). Imaging dislocations in ice. *Microscopy Research and Technique*, *62*(1), 70–82. https://doi.org/10.1002/jemt.10382Bell, I. A., Wilson, C. J. L., McLaren, A. C., & Etheridge, M. A. (1986). Kinks in mica: Role of dislocations and (001)

cleavage. *Tectonophysics*, *127*(1–2), 49–65. https://doi.org/10.1016/0040-1951(86)90078-8Bestmann, M., & Prior, D. J. (2003). Intragranular dynamic recrystallization in naturally deformed calcite marble: Diffusion accommodated grain boundary sliding as a result of subgrain rotation recrystallization. *Journal of Structural Geology*, *25*(10), 1597–1613. https://doi.org/10.1016/S0191-8141(03)00006-3Boyle, A. P., Prior, D. J., Banham, M. H., & Timms, N. E. (1998). Plastic deformation of metamorphic pyrite: New evidence from electron-backscatter diffraction and forescatter orientation-contrast imaging. *Mineralium Deposita*, *34*(1), 71–81. https://doi.org/10.1007/s001260050186De Bresser, J. H. P., Ter Heege, J. H., & Spiers, C. J. (2001). Grain size reduction by dynamic recrystallization: Can it result in major rheological weakening? *International Journal of Earth Sciences*, *90*(1), 28–45. https://doi.org/10.1007/s005310000149Burgers, J. M. (1940). Geometrical considerations concerning the structural irregularities to be assumed in a crystal. *Proceedings of the Physical Society*, *52*(1), 23–33. https://doi.org/10.1088/0959-5309/52/1/304Carlton, C. E., & Ferreira, P. J. (2007). What is behind the inverse Hall-Petch effect in nanocrystalline materials? *Acta Materialia*, *55*(11), 3749–3756. https://doi.org/10.1016/j.actamat.2007.02.021Castelnau, O., Blackman, D. K., Lebensohn, R. A., & Castañeda, P. P. (2008). Micromechanical modeling of the viscoplastic behavior of olivine. *Journal of Geophysical Research: Solid Earth*, *113*(9), 1–18. https://doi.org/10.1029/2007JB005444Chauve, T., Montagnat, M., Piazolo, S., Journaux, B., Wheeler, J., Barou, F., et al. (2017). Non-basal dislocations should be accounted for in simulating ice mass flow. *Earth and Planetary Science Letters*, *473*, 247–255.Cole, D. M. (1979). Preparation of polycrystalline ice specimens for laboratory experiments. *Cold Regions Science and Technology*, *1*(2), 153–159. https://doi.org/10.1016/0165-232X(79)90007-7Cornelius, T. W., & Thomas, O. (2018). Progress of in situ synchrotron X-ray diffraction studies on the mechanical behavior of materials at small scales. *Progress in Materials Science*, *94*, 384–434. https://doi.org/10.1016/j.pmatsci.2018.01.004Duval, P., Ashby, M. F., & Anderman, I. (1983). Rate-controlling processes in the creep of polycrystalline ice. *Journal of Physical Chemistry*, *87*(21), 4066–4074. https://doi.org/10.1021/j100244a014Fan, S., Hager, T. F., Prior, D. J., Cross, A. J., Goldsby, D. L., Qi, C., et al. (2020). Temperature and strain controls on ice deformation mechanisms: insights from the microstructures of samples deformed to progressively higher strains at −10, −20 and −30 °C. *The Cryosphere*, *14*(11), 3875–3905. https://doi.org/10.5194/tc-14-3875-2020Fan, S., Cross, A. J., Prior, D. J., Goldsby, D. L., Hager, T. F., Negrini, M., & Qi, C. (2021). Crystallographic Preferred Orientation (CPO) Development Governs Strain Weakening in Ice: Insights From High-Temperature Deformation Experiments. *Journal of Geophysical Research: Solid Earth*, *126*(12). https://doi.org/10.1029/2021JB023173Fan, S., Prior, D. J., Hager, T. F., Cross, A. J., Goldsby, D. L., & Negrini, M. (2021). Kinking facilitates grain nucleation and modifies crystallographic preferred orientations during high-stress ice deformation. *Earth and Planetary Science Letters*, *572*, 117136.

https://doi.org/10.1016/j.epsl.2021.117136Fan, S., Prior, D. J., Cross, A. J., Goldsby, D. L., Hager, T. F., Negrini, M., & Qi, C. (2021). Using grain boundary irregularity to quantify dynamic recrystallization in ice. *Acta Materialia*, *209*, 116810. https://doi.org/10.1016/j.actamat.2021.116810Faul, U. (2021). Dislocation structure of deformed olivine single crystals from conventional EBSD maps. *Physics and Chemistry of Minerals*, *48*(9), 1–15. https://doi.org/10.1007/s00269-021-01157-3Foreman, A. J. E. (1955). Dislocation energies in anisotropic crystals. *Acta Metallurgica*, *3*(4), 322–330. https://doi.org/10.1016/0001-6160(55)90036-5Goldsby, D. L., & Kohlstedt, D. L. (2001). Superplastic deformation of ice: Experimental observations. *Journal of Geophysical Research: Solid Earth*, *106*(B6), 11017–11030. https://doi.org/10.1029/2000jb900336Goldsby, D. L., & Kohlstedt, D. L. (2002). Reply to comment by P. Duval and M. Montagnat on "Superplastic deformation of ice: Experimental observations." *Journal of Geophysical Research: Solid Earth*, *107*(B11), ECV 17-1-ECV 17-5. https://doi.org/10.1029/2002jb001842Goldsby, D.L., & Kohlstedt, D. L. (1997). Grain boundary sliding in fine-grained Ice I. *Scripta Materialia*, *37*(9), 1399–1406. https://doi.org/10.1016/S1359-6462(97)00246-7Goldsby, David L. (2006). Superplastic Flow of Ice Relevant to Glacier and Ice-Sheet Mechanics. In *Glacier Science and Environmental Change* (pp. 308–314). Malden, MA, USA: Blackwell Publishing. https://doi.org/10.1002/9780470750636.ch60Goux, C. (1974). Structure des joints de grains: considérations cristallographiques et méthodes de calcul des structures. *Canadian Metallurgical Quarterly*, *13*(1), 9–31. https://doi.org/10.1179/cmq.1974.13.1.9Halfpenny, A., Prior, D. J., & Wheeler, J. (2006). Analysis of dynamic recrystallization and nucleation in a quartzite mylonite. *Tectonophysics*, *427*(1–4), 3–14. https://doi.org/10.1016/j.tecto.2006.05.016Hammes, D. M., & Peternell, M. (2018). Reconstruction of 3D grain boundaries from rock thin sections, using an advanced polarised-light microscopy method. *Journal of Microscopy*, *269*(1), 23–35. https://doi.org/10.1111/jmi.12605Hansen, L. N., Zimmerman, M. E., & Kohlstedt, D. L. (2011). Grain boundary sliding in San Carlos olivine: Flow law parameters and crystallographic-preferred orientation. *Journal of Geophysical Research: Solid Earth*, *116*(8), 1–16. https://doi.org/10.1029/2011JB008220Hansen, Lars N., Warren, J. M., Zimmerman, M. E., & Kohlstedt, D. L. (2016). Viscous anisotropy of textured olivine aggregates, Part 1: Measurement of the magnitude and evolution of anisotropy. *Earth and Planetary Science Letters*, *445*, 92–103. https://doi.org/10.1016/j.epsl.2016.04.008Heinemann, S., Wirth, R., Gottschalk, M., & Dresen, G. (2005). Synthetic [100] tilt grain boundaries in forsterite: 9.9 to 21.5°. *Physics and Chemistry of Minerals*, *32*(4), 229–240. https://doi.org/10.1007/s00269-005-0448-9Herwegh, M., & Handy, M. R. (1996). The evolution of high-temperature mylonitic microfabrics: Evidence from simple shearing of a quartz analogue (norcamphor). *Journal of Structural Geology*, *18*(5), 689–710. https://doi.org/10.1016/S0191-8141(96)80033-2Hidas, K., Tommasi, A., Mainprice, D., Chauve, T., Barou, F., & Montagnat, M. (2017). Microstructural evolution during thermal

annealing of ice-I h. *Journal of Structural Geology*, *99*(2086), 31–44. https://doi.org/10.1016/j.jsg.2017.05.001Hirth, G., & Tullis, J. (1992). Dislocation creep regimes in quartz aggregates. *Journal of Structural Geology*, *14*(2), 145–159. https://doi.org/10.1016/0191-8141(92)90053-YHirth, J. P., & Balluffi, R. W. (1973). On grain boundary dislocations and ledges. *Acta Metallurgica*, *21*(7), 929–942. https://doi.org/10.1016/0001-6160(73)90150-8Hondoh, T. (2000). Nature and behavior of dislocations in ice. *Physics of Ice Core Records*, 3–24.Hu, Y., Shu, L., Yang, Q., Guo, W., Liaw, P. K., Dahmen, K. A., & Zuo, J. M. (2018). Dislocation avalanche mechanism in slowly compressed high entropy alloy nanopillars. *Communications Physics*, *1*(1), 1–8. https://doi.org/10.1038/s42005-018-0062-zIliescu, D., Baker, I., & Chang, H. (2004). Determining the orientations of ice crystals using electron backscatter patterns. *Microscopy Research and Technique*, *63*(4), 183–187. https://doi.org/10.1002/jemt.20029Jacka, T. H., & Li, J. (2000). Flow rates and crystal orientation fabrics in compression of polycrystalline ice at low temperatures and stresses. In *International Symposium on Physics of Ice Core Records* (pp. 83–102). Hokkaido University Press. Retrieved from http://hdl.handle.net/2115/32463Kapoor, R., & Verdhan, N. (2016). Interaction of dislocation pile-up with a low-angle tilt boundary: a discrete dislocation dynamics study. *Philosophical Magazine*, *97*(7), 465–488. https://doi.org/10.1080/14786435.2016.1266102Konishi, K., Nakamura, Y., Nagae, A., Kawabata, N., Tanaka, T., Tomita, N., et al. (2020). Direct observation and three dimensional structural analysis for threading mixed dislocation inducing current leakage in 4H-SiC IGBT. *Japanese Journal of Applied Physics*, *59*(1). https://doi.org/10.7567/1347-4065/ab5ee8Li, J. C. M. (1961). High-Angle Tilt Boundary—A Dislocation Core Model. *Journal of Applied Physics*, *32*(3), 525–541. https://doi.org/10.1063/1.1736036Linckens, J., Zulauf, G., & Hammer, J. (2016). Experimental deformation of coarse-grained rock salt to high strain. *Journal of Geophysical Research: Solid Earth*, *121*(8), 6150–6171. https://doi.org/10.1002/2016JB012890Lloyd, G. E., Farmer, A. B., & Mainprice, D. (1997). Misorientation analysis and the formation and orientation of subgrain and grain boundaries. *Tectonophysics*, *279*(1–4), 55–78. https://doi.org/10.1016/S0040-1951(97)00115-7Lloyd, G. E., Lee, A. L., & Kahl, M. (2021). A practical method to determine the five-parameter orientation of intragranular boundaries in polycrystals. *Tectonophysics*, *814*(May), 228955. https://doi.org/10.1016/j.tecto.2021.228955Lopez-Sanchez, M. A., Tommasi, A., Ismail, W. Ben, & Barou, F. (2021). Dynamic recrystallization by subgrain rotation in olivine revealed by electron backscatter diffraction. *Tectonophysics*, (January), 228916. https://doi.org/10.1016/j.tecto.2021.228916Mainprice, D., Lloyd, G. E., & Casey, M. (1993). Individual orientation measurements in quartz polycrystals: advantages and limitations for texture and petrophysical property determinations. *Journal of Structural Geology*, *15*(9–10), 1169–1187. https://doi.org/10.1016/0191-8141(93)90162-4McLaren, A. C. (1991). *Transmission Electron Microscopy of Minerals and Rocks. Transmission Electron Microscopy of Minerals and Rocks*. https://doi.org/10.1017/cbo9780511529382von

Mises, R. (1928). Mechanik der plastischen Formänderung von Kristallen. *ZAMM - Zeitschrift Für Angewandte Mathematik Und Mechanik*, *8*(3), 161–185. https://doi.org/10.1002/zamm.19280080302Nabarro, F. R. . (1967). *Theory of crystal dislocations*. Oxford University Press.Nervo, L., King, A., Fitzner, A., Ludwig, W., & Preuss, M. (2016). A study of deformation twinning in a titanium alloy by X-ray diffraction contrast tomography. *Acta Materialia*, *105*, 417–428. https://doi.org/10.1016/j.actamat.2015.12.032Orowan, E. (1934). Zur Kristallplastizität. I - Tieftemperaturplastizität und Beckersche Formel. *Zeitschrift Für Physik*, *89*(9–10), 605–613. https://doi.org/10.1007/BF01341478Peach, M., & Koehler, J. S. (1950). The forces exerted on dislocations and the stress fields produced by them. *Physical Review*, *80*(3), 436–439. https://doi.org/10.1103/PhysRev.80.436Piazolo, S., Jessell, M. W., Prior, D. J., & Bons, P. D. (2004). The integration of experimental in-situ EBSD observations and numerical simulations: A novel technique of microstructural process analysis. *Journal of Microscopy*, *213*(3), 273–284. https://doi.org/10.1111/j.0022-2720.2004.01304.xPiazolo, S., Montagnat, M., & Blackford, J. R. (2008). Sub-structure characterization of experimentally and naturally deformed ice using cryo-EBSD. *Journal of Microscopy*, *230*(3), 509–519. https://doi.org/10.1111/j.1365-2818.2008.02014.xPiazolo, S., Montagnat, M., Grennerat, F., Moulinec, H., & Wheeler, J. (2015). Effect of local stress heterogeneities on dislocation fields: Examples from transient creep in polycrystalline ice. *Acta Materialia*, *90*, 303–309. https://doi.org/10.1016/j.actamat.2015.02.046Poirier, J.-P. (1985). *Creep of Crystals—High-Temperature Deformation Processes in Metals, Ceramics and Minerals*. Cambridge University Press. https://doi.org/10.1017/CBO9780511564451Poirier, J. P. (1976). On the symmetrical role of cross-slip of screw dislocations and climb of edge dislocations as recovery processes controlling high-temperature creep. *Revue de Physique Appliquée*, *11*(6), 731–738. https://doi.org/10.1051/rphysap:01976001106073100Poirier, J. P., & Nicolas, A. (1975). Deformation-Induced Recrystallization Due to Progressive Misorientation of Subgrains, with Special Reference to Mantle Peridotites. *The Journal of Geology*, *83*(6), 707–720. https://doi.org/10.1086/628163Polanyi, M. (1934). Über eine Art Gitterstörung, die einen Kristall plastisch machen könnte. *Zeitschrift Für Physik*, *89*(9–10), 660–664. https://doi.org/10.1007/BF01341481Prior, D. J. (1999). Problems in determining the misorientation axes, for small angular misorientations, using electron backscatter diffraction in the SEM. *Journal of Microscopy*, *195*(3), 217–225. https://doi.org/10.1046/j.1365-2818.1999.00572.xPrior, D.J., Lilly, K., Seidemann, M., Vaughan, M., Becroft, L., Easingwood, R., et al. (2015). Making EBSD on water ice routine. *Journal of Microscopy*, *259*(3), 237–256. https://doi.org/10.1111/jmi.12258Prior, David J., Wheeler, J., Peruzzo, L., Spiess, R., & Storey, C. (2002). Some garnet microstructures: An illustration of the potential of orientation maps and misorientation analysis in microstructural studies. *Journal of Structural Geology*, *24*(6–7), 999–1011. https://doi.org/10.1016/S0191-8141(01)00087-6Read, W. T., & Shockley, W. (1950). Dislocation Models of Crystal Grain Boundaries. *Physical Review*,

78(3), 275–289. https://doi.org/10.1103/PhysRev.78.275Reddy, S. M., & Buchan, C. (2005). Constraining kinematic rotation axes in high-strain zones: A potential microstructural method? *Geological Society Special Publication*, *243*, 1–10. https://doi.org/10.1144/GSL.SP.2005.243.01.02de Riese, T., Evans, L., Gomez-Rivas, E., Griera, A., Lebensohn, R. A., Llorens, M. G., et al. (2019). Shear localisation in anisotropic, non-linear viscous materials that develop a CPO: A numerical study. *Journal of Structural Geology*, *124*(January), 81–90. https://doi.org/10.1016/j.jsg.2019.03.006Rutter, E. H. (1999). On the relationship between the formation of shear zones and the form of the flow law for rocks undergoing dynamic recrystallization. *Tectonophysics*, *303*(1–4), 147–158. https://doi.org/10.1016/S0040-1951(98)00261-3Saylor, D. M., Morawiec, A., & Rohrer, G. S. (2003). The relative free energies of grain boundaries in magnesia as a function of five macroscopic parameters. *Acta Materialia*, *51*(13), 3675–3686. https://doi.org/10.1016/S1359-6454(03)00182-4Seidemann, M., Prior, D. J., Golding, N., Durham, W. B., Lilly, K., & Vaughan, M. J. (2020). The role of kink boundaries in the deformation and recrystallisation of polycrystalline ice. *Journal of Structural Geology*, *136*(October 2017), 104010. https://doi.org/10.1016/j.jsg.2020.104010Sheinerman, A. G., Castro, R. H. R., & Gutkin, M. Y. (2020). A model for direct and inverse Hall-Petch relation for nanocrystalline ceramics. *Materials Letters*, *260*, 126886. https://doi.org/10.1016/j.matlet.2019.126886Shigematsu, N., Prior, D. J., & Wheeler, J. (2006). First combined electron backscatter diffraction and transmission electron microscopy study of grain boundary structure of deformed quartzite. *Journal of Microscopy*, *224*(3), 306–321. https://doi.org/10.1111/j.1365-2818.2006.01697.xSkemer, P., Warren, J. M., Kelemen, P. B., & Hirth, G. (2009). Microstructural and rheological evolution of a mantle shear zone. *Journal of Petrology*, *51*(1–2), 43–53. https://doi.org/10.1093/petrology/egp057Stechmann, G., Zaefferer, S., Konijnenberg, P., Raabe, D., Gretener, C., Kranz, L., et al. (2016). 3-Dimensional microstructural characterization of CdTe absorber layers from CdTe/CdS thin film solar cells. *Solar Energy Materials and Solar Cells*, *151*, 66–80. https://doi.org/10.1016/j.solmat.2016.02.023Taylor, G. I. (1934). The mechanism of plastic deformation of crystals. Part I.—Theoretical. *Proceedings of the Royal Society of London. Series A, Containing Papers of a Mathematical and Physical Character*, *145*(855), 362–387. https://doi.org/10.1098/rspa.1934.0106Tokita, S., Kokawa, H., Sato, Y. S., & Fujii, H. T. (2017). In situ EBSD observation of grain boundary character distribution evolution during thermomechanical process used for grain boundary engineering of 304 austenitic stainless steel. *Materials Characterization*, *131*(January), 31–38. https://doi.org/10.1016/j.matchar.2017.06.032Trimby, P. W., Prior, D. J., & Wheeler, J. (1998). Grain boundary hierarchy development in a quartz mylonite. *Journal of Structural Geology*, *20*(7), 917–935. https://doi.org/10.1016/S0191-8141(98)00026-1Tullis, J., & Yund, R. A. (1985). Dynamic recrystallization of feldspar: A mechanism for ductile shear zone formation. *Geology*, *13*(4), 238. https://doi.org/10.1130/0091-7613(1985)13<238:DROFAM>2.0.CO;2Underwood, E. E. (1973). Quantitative

Stereology for Microstructural Analysis. *Microstructural Analysis*, *V*, 35–66. https://doi.org/10.1007/978-1-4615-8693-7_3Urai, J. L., Means, W. D., & Lister, G. S. (1986). Dynamic recrystallization of minerals. In *Mineral and Rock Deformation: Laboratory Studies* (Vol. 36, pp. 161–199). https://doi.org/10.1029/GM036p0161Valcke, S. L. A., Pennock, G. M., Drury, M. R., & De Bresser, J. H. P. (2006). Electron backscattered diffraction as a tool to quantify subgrains in deformed calcite. *Journal of Microscopy*, *224*(3), 264–276. https://doi.org/10.1111/j.1365-2818.2006.01698.xVaughan, M. J. H. (2017). *The creep behaviour, and elastic and anelastic properties of polycrystalline ice*. University of Otago.Wallis, D., Hansen, L. N., Ben Britton, T., & Wilkinson, A. J. (2016). Geometrically necessary dislocation densities in olivine obtained using high-angular resolution electron backscatter diffraction. *Ultramicroscopy*, *168*(2016), 34–45. https://doi.org/10.1016/j.ultramic.2016.06.002Wang, M. J., Sun, C. Y., Fu, M. W., Liu, Z. L., & Qian, L. Y. (2020). Study on the dynamic recrystallization mechanisms of Inconel 740 superalloy during hot deformation. *Journal of Alloys and Compounds*, *820*. https://doi.org/10.1016/j.jallcom.2019.153325Weertman, J. (1965). The Peach–Koehler equation for the force on a dislocation modified for hydrostatic pressure. *Philosophical Magazine*, *11*(114), 1217–1223. https://doi.org/10.1080/14786436508224930Weikusat, I., Kuiper, E.-J. N., Pennock, G. M., Kipfstuhl, S., & Drury, M. R. (2017). EBSD analysis of subgrain boundaries and dislocation slip systems in Antarctic and Greenland ice. *Solid Earth*, *8*(5), 883–898.Wheeler, J., Prior, D. J., Jiang, Z., Spiess, R., & Trimby, P. W. (2001). The petrological significance of misorientations between grains. *Contributions to Mineralogy and Petrology*, *141*(1), 109–124. https://doi.org/10.1007/s004100000225Wheeler, J, Mariani, E., Piazolo, S., Prior, D. J., Trimby, P., & Drury, M. R. (2009). The weighted Burgers vector: a new quantity for constraining dislocation densities and types using electron backscatter diffraction on 2D sections through crystalline materials. *Journal of Microscopy*, *233*(3), 482–494.Wheeler, John, Jiang, Z., Prior, D. J., Tullis, J., Drury, M. R., & Trimby, P. W. (2003). From geometry to dynamics of microstructure: Using boundary lengths to quantify boundary misorientations and anisotropy. *Tectonophysics*, *376*(1–2), 19–35. https://doi.org/10.1016/j.tecto.2003.08.007White, S. (1976). The Effects of Strain on the Microstructures, Fabrics, and Deformation Mechanisms in Quartzites. *Philosophical Transactions of the Royal Society A: Mathematical and Physical Sciences*, *283*(1312), 69–86. Retrieved from https://www.jstor.org/stable/74630Wilson, C. J. L., Peternell, M., Piazolo, S., & Luzin, V. (2014). Microstructure and fabric development in ice: Lessons learned from in situ experiments and implications for understanding rock evolution. *Journal of Structural Geology*, *61*, 50–77. https://doi.org/10.1016/j.jsg.2013.05.006